TITLE

Cryogenic Electron Tomography Redefines Herpesvirus Capsid Assembly Intermediates Inside the Cell Nucleus.

AUTHORS

Stefan L. Oliver[1*], Muyuan Chen[1], Leeya Engel[2], Corey W. Hecksel[1,3], Xueting Zhou[1,4], Michael F. Schmid[1], Ann M. Arvin[5,6], and Wah Chiu[1,6,7].

[1]Division of Cryo-EM and Bioimaging SSRL, SLAC National Accelerator Laboratory, Menlo Park, CA, 94025, USA. [2]Technion Israel Institute of Technology, Haifa, Israel. [3]Present address Merck Research Laboratories, Merck and Co., Rahway, NJ 07033, USA. [4]Present address Verna and Marrs McLean Department of Biochemistry and Molecular Pharmacology, Baylor College of Medicine, Houston, TX 77030, USA. Departments of [5]Pediatrics, [6]Microbiology and Immunology, and [7]Bioengineering, Stanford University School of Medicine, Stanford, CA, 94305, USA.

[*]Corresponding author: sloliver@stanford.edu

Running Title: Cryo-FIB/Cryo-ET of VZV particles.

Key words: Herpesvirus; Varicella-Zoster Virus; capsid; cryo-FIB; cryo-ET; capsid vertex specific component.

ABSTRACT

Herpesviruses encapsulate their double-stranded DNA (dsDNA) genomes within an icosahedral nucleocapsid formed in the infected cell nucleus. Four biochemically purified nucleocapsids have been characterized, but their roles in herpesvirus replication remain controversial. The status of the capsid vertex-specific component (CVSC), essential for capsid stability and dsDNA packaging and retention, is also unclear. By integrating cryogenic focused ion beam milling with electron tomography and subtomogram averaging, we derived atomic models for all protein components, including the CVSC, across different herpesvirus capsid types within infected cell nuclei. Focused classification of pentonal vertex densities revealed differences in CVSC occupancy between genome-filled capsids and capsids lacking dsDNA, highlighting structural heterogeneity and providing insight into distinct capsid assembly stages *in situ*. These intra-nuclear findings redefine the maturation model of herpesvirus capsid assembly, advancing the understanding of herpesvirus replication, and demonstrate the effectiveness of *in situ* electron imaging by studying virus assembly within host cells.

41 **INTRODUCTION**

42 The *Herpesviridae* encompass a large family of viruses comprised of alpha-, beta- and gamma
43 subgenera that infect humans and most animal species with wide ranging health and economic
44 consequences [1-8]. Varicella-zoster virus (VZV), a human alphaherpesvirus, causes varicella
45 (chicken pox) as the primary infection, and zoster (shingles) after reactivation from latency in
46 sensory ganglia[1], and can be life threatening in immunocompromised patients [9-15]. VZV vaccines
47 have reduced morbidity substantially [16-18] and antiviral drugs are effective but neither prevent VZV
48 latency in sensory neurons [19,20] or post-herpetic neuralgia after zoster [21,22], and antiviral resistance
49 can emerge [23,24]. The other two human alphaherpesviruses, herpes simplex virus (HSV) 1 and 2
50 (HSV-2), also create a significant disease burden [25,26]. HSV vaccines are not available and HSV
51 persists in neurons despite antiviral treatment [8]. Vulnerable populations need new interventions
52 for these viruses and against the betaherpesvirus, human cytomegalovirus [4], and the Epstein-Barr
53 and Kaposi's sarcoma gammaherpesviruses, which cause a range of cancers [2,3].

54 Herpesviruses are classified by their distinct 4-layer morphology composed of a double stranded
55 DNA (dsDNA) core, capsid, tegument, and envelope [27]. These complex entities form through a
56 convoluted morphogenesis process starting inside the infected cell nucleus. The dsDNA genome
57 is packaged into newly synthesized capsids that exit the nucleus across nuclear membranes into
58 the cytoplasm, where they traffic to sites of secondary envelopment, completing acquisition of
59 tegument proteins and the lipid envelope containing virus glycoproteins. The nascent enveloped
60 particles are transported in vesicular structures to the plasma membrane and released into the
61 extracellular milieu. The glycoproteins protruding from the lipid membrane then mediate virus
62 entry into neighboring cells and tegument proteins support the intracellular transport of capsids to
63 nuclear pores where the dsDNA genome is injected; additional tegument proteins undergo nuclear
64 translocation to initiate transcription factor functions. Since the herpesvirus capsid structure is
65 essential for virus genome preservation during infection, high-resolution information about the
66 progression of capsid assembly holds great potential to identify novel targets for next generation
67 pharmaceutical interventions and vaccines.

68 Herpesvirus capsids are ~125nm in diameter and share a common icosahedral symmetry with a
69 T=16 geometry made up of 60 asymmetric units. The capsid assembles in the nucleus from 161
70 capsomeres, composed of 150 hexons and 11 pentons that form an icosahedron with 12 vertices,

71 including a unique portal vertex for the packaging of the dsDNA genome and its release through
72 the host cell nuclear pore in newly infected cells. Capsids undergo several transformative stages
73 starting with immature pro-capsids, which are thought to form as capsomeres coalesce with the
74 scaffold protein to produce segments and subsequently spherical capsids [28,29]. Maturation of pro-
75 capsids occurs as the scaffold protein is proteolytically digested by its companion protease,
76 triggering a conformational change from a more spherical shape to their final icosahedral
77 morphology, with 20 flat triangular faces and 30 edges. Mature capsids have been conventionally
78 classified as A-, B-, and C-capsids, as they differ in their buoyant densities and morphologies by
79 thin section electron microscopy (EM) [30]. The cavities of C-capsids contain packaged dsDNA
80 genomes, whereas B-capsids have persistent scaffold protein and its associated protease, and A-
81 capsids are described as empty. While A- and B-capsids have been presumed to be dead-end
82 assembly products [29], an alternative hypothesis is that one or both might represent assembly
83 intermediates with the potential to encapsidate dsDNA genomes [31]. Capsid purification can induce
84 artefacts, such as loss of genomic DNA by disruption of the portal vertex cap, creating empty A-
85 capsids from C-capsids [32]. B-capsids accumulated when unit length genome formation was
86 blocked by drug inhibition of the genome-transferase complex [31], suggesting that scaffold protein
87 removal is linked to dsDNA insertion, and capsids with scaffold protein in the cavity might be
88 capsid intermediates rather than representing a failure of genome encapsidation.

89 The proteins that assemble to create a mature herpesvirus capsid have orthologues in all
90 *Herpesviridae*. These include the major capsid protein (MCP), the small capsomere interacting
91 protein (SCP), and the capsid triplex proteins 1 (TRX1) and 2 (TRX2). The multimeric subunits
92 formed by these proteins to produce fully mature capsids have been described at near atomic
93 resolution for all three subfamilies of herpesviruses [33-43]. Briefly, the MCP forms the capsomeres
94 of hexons and pentons of the icosahedral capsid. Six copies of the SCP decorate the tops of the
95 hexons. Heterotrimeric triplexes (TRX1 monomer and TRX2 dimer) occupy the canyons between
96 the capsomere towers and cover up the holes in the MCP floor to stabilize the capsid for dsDNA
97 genome containment [33,44]. At each of the 12 capsid vertices, five copies of the capsid vertex
98 specific component (CVSC) bind to triplexes adjacent to the pentons and the unique portal vertex
99 [33]. In HSV, the CVSC is a heteropentamer composed of orthologues shared with VZV; the capsid
100 vertex-specific component 1 (CVC1) monomer, two copies of CVC2, and two copies of the protein
101 designated VP1/2. CVSC binding has been associated with reinforcing capsid stability to

102 withstand the very high packaging pressure of the dsDNA genome [45-47]. At the portal vertex, a
103 dodecamer (VZV ORF54; HSV-1 pUL6), replaces a penton with a portal and tentacle-like helices
104 that ring the DNA translocation channel, and an ATP-driven terminase is recruited to cleave the
105 herpesvirus dsDNA genome for packaging [29,34-36,38,45,48-50]. The CVSC is expected to form part of
106 the portal cap that retains the dsDNA genome in the capsid [29,34-36,38,45,48-50]. The CVSC
107 heteropentamer has also been called the capsid-associated tegument complex because its subunits
108 include the large tegument protein (VP1/2), VZV ORF22 and HSV pUL36 [51]; in HSV and PRV,
109 these orthologues have been identified as inner tegument proteins that function in microtubule-
110 mediated capsid transport to cell nuclei [52,53]. The CVSC of CMV, a betaherpesvirus, has a non-
111 conserved tegument subunit, pp150 [42,54], while gammaherpesvirus CVSCs are thought to resemble
112 those of the alphaherpesviruses [51].

113 Critical information about the structural composition of herpesvirus capsids was gained using
114 cryogenic-electron tomography (cryo-ET) of purified particles but resolution was limited [55-63]. The
115 adaptation of single particle cryo-EM enabled capsid structures of most human herpesviruses to
116 be determined at better than 4Å resolution [33,35-41,47]. However, knowledge about capsid assembly
117 as it occurs *in situ* within the infected cell nucleus remains limited. The CVSC has been proposed
118 to associate with the capsid inside the infected cell nucleus, but the structural organizations of their
119 individual components have not been visualized directly in the nucleus of herpesvirus infected
120 cells [64,65]. Whether the assembly of the VP1/2 subunit of the CVSC takes place in the nucleus or
121 cytoplasm is unclear [64,66,67]. Furthermore, despite previous high-resolution structures for VZV
122 capsids, the CVSC and the portal vertex were not resolved in these studies [39,41]. Recent work with
123 purified capsids partially resolved the CVSC and the portal vertex [68]. To better understand capsid
124 assembly and the relationship between capsids conventionally classified as A- and B-capsid types
125 compared to the dsDNA containing C-capsids, we sought subnanometer resolution imaging of
126 capsids within VZV infected cells. Imaging inside mammalian cells is challenging because cell
127 thickness limits the penetration of the electron beam and reduces the image contrast due to inelastic
128 scattering and multiple electron scattering [69]. Even at high voltages (1MV), the electron beam can
129 only penetrate 1µm; the nuclei of typical mammalian cells range in size from 5 to 10µm. To
130 overcome this limitation, recent advances in cryogenic focused ion beam and scanning electron
131 microscopy (cryo-FIB/SEM) have been introduced to mill away most of the thick and vitrified
132 cell, leaving a thin lamella of 100 to 400 nm in thickness. When integrated with cryo-ET using a

133 300 keV electron microscope, 3D volumes can be produced at near-atomic resolution by imaging
134 at different angles, cryo-ET reconstruction, and subtomogram averaging (STA) [70]. We applied
135 this approach to visualize VZV particles within infected cells in a frozen, hydrated state, without
136 the use of contrast agents, and determined the structures of their component proteins.

137 Our findings reveal that the CVSC heteropentamer assembles on capsids in the nucleus of infected
138 cells and that the definition of the asymmetric unit of the icosahedral VZV capsid should be
139 expanded to incorporate the CVSC interactions with neighboring MCPs and triplexes, which were
140 absent from previous capsid models [39,41]. Focused classification, including of the unique portal
141 vertex, indicates that genome-filled C-capsids have full CVSC occupancy, defined as the
142 maximum of five heteropentamers. Among capsids lacking dsDNA, empty A-capsids were not
143 detected within the infected cell nucleus whereas capsid assembly intermediates (CAIs) could be
144 distinguished by differences in the number of CVSCs found at the vertices of the icosahedron,
145 which correlated with levels of scaffold protein in the capsid cavity, suggesting a continuum along
146 the assembly pathway. Notably, CAIs would be grouped together as B-capsids based on scaffold
147 protein alone. These observations provide evidence that CVSC acquisition can serve as a temporal
148 marker for the progression of intra-nuclear herpesvirus capsid assembly *in situ*, consistent with its
149 biological importance for ensuring the stability of genome-containing capsids during nuclear
150 egress and formation of complete virus particles in the cytoplasm.

151 **RESULTS**

152 **VZV morphogenesis visualized within infected cells *in situ* by cryo-FIB-SEM and cryo-ET.**

153 To visualize herpesvirus morphogenesis in 3D-space, a workflow was developed to distribute VZV
154 infected cells evenly on EM grids suitable for cryo-FIB milling. First, because VZV does not yield
155 high titer cell-free virus particles [1], it was critical to optimize the passage of infected cells onto
156 uninfected cells to initiate infection prior to vitrification. Infection was monitored by the
157 fluorescence RFP signal produced by MeWo cells infected with a recombinant VZV (pOka-TK-
158 RFP [71]) expressing a thymidine kinase (TK) tagged with a monomeric red fluorescence protein
159 (RFP; **Fig. 1**); the pOka-TK-RFP maintains the characteristics of the bacterial artificial
160 chromosome derived WT pOka [71-74]. Second, to overcome the propensity of VZV infected cells
161 to adhere to the grid bars when seeded on SiO_2 EM grids, islands of extracellular matrix were
162 micropatterned within the grid squares (**Fig. 1b**). With this technique, infected cells were

163 positioned centrally within the grid squares after vitrification and ideal for cryo-FIB milling to
164 produce lamella suitable for cryo-ET (**Fig. 1c and 1d**). Tomograms of cryo-FIB milled cells
165 revealed the complex cellular environment in VZV infected cells (**Fig. 1e; Suppl. Fig. 1 to 7;**
166 **Suppl. Table 1 and 2**). Cellular features were readily visible in medium magnification (16.9 to
167 39.1Å/pixel) montage maps used to facilitate cryo-ET tilt series data collection from cells thinned
168 to a target thickness of ~175nm; the nuclear envelope with visible nuclear pores demarcated the
169 intranuclear and cytoplasmic compartments (**Fig. 1d; Suppl. Fig. 1a, 3a to 7a**). A plethora of
170 vesicular structures, mitochondria, and, within infected cells, VZV capsids and complete virus
171 particles, was visible, facilitating the localization of regions of interest in a tilt series collection.
172 The higher resolution tomographic reconstructions yielded substantial contrast enabling machine
173 learning-based segmentation to identify ribosomes, microtubules, microfilaments, complex
174 vesicular structures, and assembled capsids in the nucleus and sites of virus particle morphogenesis
175 in the cytoplasm (**Suppl. Fig. 7c**).

176 Several critical steps in the herpesvirus replication cycle were captured within cryo-ET tomograms
177 generated from cryo-FIB milled cells infected with VZV (**Fig. 1e; Suppl. Fig. 1 to 8; Suppl.**
178 **Movie 1 to 6**). These included capsids docked at the nuclear pore (**Fig 1ei; Suppl. Fig 1; Suppl.**
179 **Movie 1**), newly synthesized capsids in the nucleus (**Fig 1eii; Suppl. Fig 3; Suppl. Movie 2**),
180 nuclear egress (**Fig 1eiii; Suppl. Fig 4; Suppl. Movie 3**), secondary envelopment (**Fig 1eiv;**
181 **Suppl. Fig 5; Suppl. Movie 4**), VZV particle morphogenesis (**Fig 1ev; Suppl. Fig. 6 and 7;**
182 **Suppl. Movie 5**), and VZV particles bound to the extracellular plasma membrane surface (**Fig**
183 **1evi; Suppl. Fig 8; Suppl. Movie 6**), a typical feature of this cell associated virus [1]. Within the
184 infected cell nucleus, pro-capsids and A-, B-, and C-capsids based on conventional morphological
185 features, were distinguishable in 3D-space at this resolution. Procapsids were spherical and
186 contained a solid density of scaffold protein; capsids apparently devoid of scaffold protein or
187 dsDNA (conventional A-capsids) were identified; B-capsids were observed and defined by the
188 presence of scaffold protein (**Fig. 1eii**); and C-capsids were distinguishable by their cavities filled
189 with dsDNA (**Fig. 1eiii, 2A and 2B; Suppl. Fig. 4 to 6**). Procapsid assembly precursors were
190 identified within infected cell nuclei, appearing as angular segments of capsomeres associated with
191 scaffold protein with a curvature similar to the procapsids (**Suppl. Fig. 2**). Importantly, high-
192 resolution detail was evident by the visualization of individual capsid capsomeres (**Fig 1eii, Suppl.**
193 **Fig 3; Suppl. Movie 2**), individual nuclear egress complexes (**Fig 1eiii, Suppl. Fig 4; Suppl.**

194 **Movie 3**), and individual glycoproteins on enveloped VZV particles in the cytoplasm or bound to
195 the plasma membrane (**Fig. 1eiv and vi; Suppl. Fig. 5, 8 and 9; Suppl. Movie 5 and 6**). Partially
196 assembled virus particles were observed within cytoplasmic sites of VZV secondary envelopment
197 and morphogenesis, including sites of tegument protein accumulation, based on the electron dense
198 protein surrounding the capsids within the reconstructed tomograms (**Fig. 1eiv and 1ev; Suppl.**
199 **Fig. 5 and 6**). For example, a VZV light particle, a glycoprotein-studded envelope containing
200 tegument proteins but without a capsid, and a complete particle were observed in a vesicular
201 structure, and in a neighboring vesicular structure, an elongated VZV particle contained a C-capsid
202 and the accumulation of tegument protein associated with a membranous structure (**Suppl. Fig.**
203 **7b**). The virus envelope within these vesicular structures was detected by machine learning-based
204 segmentation (**Suppl. Fig. 7c**). Collectively, these direct visualizations reveal details of the VZV
205 replication cycle previously unobserved in its native hydrated state inside infected cells,
206 particularly for nuclear egress, tegument acquisition during secondary envelopment, and virus
207 glycoprotein interactions with both intra- and extracellular membranes.

208 **Subnanometer reconstruction of VZV capsid proteins in infected cells.**

209 From 194 tilt series, 1,084 capsids were identified and classified based on classical morphological
210 features, the presence or absence of scaffold protein or the virus genome in the capsid cavity. A
211 visual inspection of the image contrast in the capsid cavity revealed a continuum of sparse density,
212 likely scaffolding, suggesting that completely empty A-capsids are absent or very rare within
213 infected cell nuclei (**Suppl. Fig. 10**). Residual scaffold protein was limited enough in some capsids
214 to be obscured by conventional EM techniques due to the plane of the cut in ultrathin sections in
215 previous studies. The cellular distribution of the 1,084 VZV capsids was primarily localized inside
216 the nucleus (n=980) with only 9.3% detected in the cytoplasm either as naked capsids, without
217 tegument or envelope proteins (n=42), or as complete enveloped VZV particles (n=59) (**Suppl.**
218 **Table 3**). The capsid distribution was typical for peak particle synthesis of VZV infected cells,
219 which aligns with thymidine kinase (TK) expression, an early gene, as determined by the red
220 fluorescence signal produced from the recombinant pOka-TK-RFP virus.

221 An initial 13Å cryo-ET map of the VZV capsid was generated by subtomogram averaging (STA)
222 of 317 capsids (**Fig. 2; Suppl. Fig. 11**), containing variable quantities of scaffold protein or
223 packaged DNA. This icosahedral symmetry-imposed map clearly shows the T=16 icosahedron,

224 composed of 60 asymmetric units. Each asymmetric unit consists of a single pentonal MCP
225 subunit (P^P), one peripentonal hexon (P), one central hexon (C), and half of an edge hexon (E),
226 along with interdigitating triplexes (Ta, Tb, Tc, Td, and Te) (**Fig. 2c and 2d**). Cryo-ET maps were
227 produced for the vertex around the 5-fold axis (8.3Å) and the 3-fold symmetry axis (8.4Å) by
228 subsequent symmetry expansion and focused refinement of the 317 capsids. (**Fig. 2e and 2f;**
229 **Suppl. Fig. 11**). The 8.3Å vertex map had sufficient resolution to perform segmentation of
230 individual proteins for the pentonal MCP (P^P), six MCPs (P^{1-6}) for the peripentonal hexon and the
231 associated small capsomere interacting protein (SCP), triplex proteins TRX1 (monomer) and
232 TRX2 (dimer) that form the $\alpha_2\beta$ heterotrimers of Ta and Tc, and the three proteins, CVC1 (ORF43
233 monomer), CVC2 (ORF34 dimer), and ORF22 dimer, that assemble to form the capsid vertex
234 specific component (CVSC) heteropentamer (**Fig. 3 and 4; Suppl. Table 4**). Similar to the vertex
235 map, individual proteins were segmented for the 8.4Å 3-fold symmetry axis cryo-ET map for the
236 six MCPs (C^{1-6}) for the central hexon and associated SCP in addition to the TRX1 and TRX2
237 proteins of the Te triplex (**Suppl. Fig. 12**). The densities in both 3- and 5-fold axes of symmetry
238 were segmented using the structure derived from single particle cryo-EM of VZV capsids
239 (7BW6)[39]. All of the features for the pentonal, peripentonal hexon, and central hexon MCPs were
240 apparent, including the tower, consisting of the crown and buttress regions (**Fig. 3a to c; Suppl.**
241 **Fig. 12**), and the HK97 phage capsid protein-like fold facing the interior chamber of the capsid
242 (**Fig. 3d**), which is evolutionary conserved for herpesviruses and dsDNA bacteriophages [75]. The
243 resolution of these regions in the cryo-ET map was supported by the ability to observe densities
244 for alpha helices in each of the MCP, TRX1 and TRX2 proteins and corresponding Map-Q scores
245 (**Fig. 3c; Suppl. Fig. 12c and e; Suppl. Fig. 13; Suppl. Movie 7**). The classical HK97 phage
246 capsid protein fold of the MCP was distinguishable with the long alpha helix (helix 4)
247 interdigitating at the pseudo 3-fold axis of symmetry between the penton and neighboring
248 peripentonal hexon MCPs (**Fig. 3d**). These subnanometer resolution structural details of the MCP,
249 SCP, TRX1 and TRX2 are the first to be visualized inside the nucleus of a herpesvirus-infected
250 cell.

251 **The CVSC heteropentamer assembles as part of the capsid asymmetric unit in infected cell**
252 **nuclei.**

253 The CVSC status as a capsid component has been difficult to assess due to its propensity to
254 disassociate from vertices during herpesvirus capsid purification, including VZV [45,76,39,41]. In

255 contrast, the CVSC density was apparent at all 12 vertices of the capsid structure in infected cell
256 nuclei (**Fig. 2c**). Furthermore, the 8.3Å cryo-ET map of the VZV capsid vertex was of sufficient
257 resolution to extract densities for the CVSC, demonstrating that the heteropentamer is a capsid
258 component acquired independently of the full tegument layer of the virus particle (**Figs. 2e, 4a**
259 **and 4c**). An AlphaFold model of the CVSC structure oriented the head group for each CVC2
260 (ORF34) molecule at a downward angle compared to the extracted CVSC cryo-ET map density
261 (**Suppl. Fig. 14a and 14b**). The CVC2 head group AlphaFold models were fitted into the cryo-
262 EM density with the aid of molecular dynamics flexible fitting (**Suppl. Fig. 14c; Suppl. Movie**
263 **8**), enabling segmentation of the cryo-EM density into the five individual subunits of the CVSC
264 heteropentamer (**Fig. 4a to 4c**). This revealed that the CVC1 subunit (ORF43 monomer), which
265 has a limited interaction with TRX1 from triplex Te, primarily associates with all three Ta triplex
266 subunits along with MCP P^1 and P^2 of the peripentonal hexon from the neighboring asymmetric
267 unit (**Fig. 4b, 4d and 4e**). A helical bundle forms between the CVC1 subunit, the two ORF22
268 proteins and the two CVC2 proteins, enabling the CVC2 head group to interact with the
269 peripentonal hexon facing side of the pentonal MCP crown (**Fig. 4a**). Since almost all capsids
270 analyzed were intra-nuclear, these observations definitively demonstrate that CVSC assembly at
271 the capsid vertices occurs inside the nucleus. Furthermore, these findings enabled us to redefine
272 the asymmetric unit of the mature C-capsid to be composed of six C hexon subunits (MCP and
273 SCP), three E hexon subunits, and a pair of three peripentonal hexon subunits from neighboring
274 hexons, one pentonal MCP, five interdigitating triplexes, and a single CVSC heteropentamer (**Fig.**
275 **2d and 4b; Suppl. Fig. 15a**). This arrangement differs from previous models of alphaherpesvirus
276 asymmetric units, where the interaction between CVC1 with triplexes Ta and Tc and MCP P^1 and
277 P^2 were not used to define the asymmetric unit, proteins were missing, or proteins from a
278 neighboring asymmetric unit were included (**Suppl. Fig. 15**).

279 **CVSC acquisition redefines capsid assembly intermediates formed during herpesvirus**
280 **capsid assembly.**

281 Given uncertainties about the stages of capsid assembly based on studies of purified capsids [45,76,77]
282 [31,78], we investigated the distribution of CVSC heteropentamers at vertices of capsids in infected
283 cells to determine whether the CVSC occupancy could be used to differentiate capsid types and
284 achieve a more precise characterization for the stages of capsid assembly (**Fig. 5**). Uniform
285 Manifold Approximation and Project (UMAP) is a dimension reduction technique that can be used

286 for the visualization and categorization of complex data [79], including structural heterogeneity in
287 single particle Cryo-EM [80,81]. Application of this unsupervised computational approach (**Fig. 5a**)
288 using three-axis orthogonal projection in latent space classified the 317 capsids that were used to
289 generate the 8.3Å vertex cryo-ET map (**Fig. 2**). Each capsid image was aligned to its symmetry
290 axes, and icosahedral symmetry was applied to individual particles before the projections were
291 generated to compensate for the missing wedge effect intrinsic to cryo-ET data [82]. Three clusters
292 were differentiated in latent space, revealing limited versus (i) extensive (ii) scaffold protein in the
293 capsid cavity, and those with packaged DNA (iii) corresponding to C-capsids, as viewed along the
294 2-, 3-, and 5-fold axes of symmetry and the STA for each class (**Fig. 5a to 5c**). The detection of
295 limited quantities of scaffold protein for class i capsids enabled the differentiation from
296 conventionally designated B-capsids. The absence of any density inside the capsid cavity,
297 previously established for classical empty A-capsids based on conventional negative stained
298 images [30], was not detected within infected cell nuclei. Residual scaffold protein was visible in
299 the native structures preserved by vitrification performed in this study (**Suppl. Fig. 10**). In addition
300 to capsid cavity content differences, the three UMAP capsid clusters were found to differ in CVSC
301 occupancy at the vertices (**Fig. 5d to 5f**). For each of the 317 capsids, sub-particles were extracted
302 from the 12 vertices and aligned to the same C5 symmetry axis. These particles were initially
303 subject to binary reference free focused classification, resulting in two classes reflecting vertices
304 without or with CVSC occupancy (**Fig. 5d and 5e**). The CVSC was either absent or present, with
305 the arms and lobes of the CVSC clearly visible in the C5 symmetry STA maps (**Fig. 5d**). Capsid
306 vertices were then classified into those without and with the CVSC and by their UMAP cluster, i
307 to iii (**Fig. 5e**). As expected, CVSC occupancy was highest on C-capsids in infected cells, as has
308 been reported for purified capsids [33,37,40,42,47], and because they are considered complete and ready
309 for egress from the nucleus for final tegumentation and envelopment in the cytoplasm [45]. Persistent
310 scaffold protein is the conventional marker for B-capsids by EM, resulting in greater buoyant
311 density than empty A-capsids [30]. Notably, capsids differed in CVSC occupancy depending on
312 whether scaffold protein was limited or extensive within the capsid cavity, with the former having
313 greater CVSC occupancy than the latter (**Fig. 5b to 5f**). Critically, for the 12 vertices of individual
314 capsids, CVSC occupancy at each vertex increased with decreasing levels of scaffold protein
315 density (**Fig. 5f**). Since C-capsids have the highest CVSC occupancy, these findings indicate that
316 capsids with relatively more CVSC occupancy and less scaffold protein are capsid assembly

317 intermediates (CAIs) further along the pathway of capsid maturation than those with less CVSC
318 occupancy and more residual scaffold protein.

319 To further scrutinize the CVSC on capsids in infected cells, vertex particles were subjected to C5
320 symmetry expansion, generating five sub-particles for the asymmetric orientations. Additional
321 focused classification using a mask covering a single CVSC site produced two classes of CVSC
322 occupancy at each individual location, those with or without the heteropentamer. This procedure
323 established the frequency of CVSC heteropentamers, producing vertex sub-particles with either
324 zero copies, 1 to 5 copies, or 2 and 3 copies of non-consecutive CVSC distribution, which were
325 used for STA without symmetry imposed (**Fig. 5g and 5h**). Each capsid has a potential maximum
326 of 60 copies of the CVSC heteropentamer, as there are 12 capsid vertices and 5 CVSC per vertex,
327 including the portal vertex [29,34-36,38,45,48-50]. For the 317 capsids in the present study, there were
328 3,804 vertices. Frequencies ranged from 290 vertices without a CVSC to 1,198 vertices with a
329 full complement of five copies of the CVSC (**Fig. 5g**). Additionally, alternative distributions of
330 the CVSC were observed at vertices where 2 or 3 copies of the heteropentamer were not adjacent
331 to one another, indicating a non-cooperative attachment of the heteropentamer to these capsid
332 vertices (**Fig. 5h**). In contrast to purified VZV C-capsids [41], intranuclear C-capsids in infected
333 cells had almost complete vertex occupancy (52; SEM = 0.861), demonstrating their maturity (**Fig.
334 5i**). CAIs with limited scaffold protein had greater CVSC occupancy (39; SEM = 0.859) compared
335 to CAIs with extensive scaffold protein (32; SEM = 0.753), providing additional evidence that the
336 former represent a stage closer to DNA encapsidation while the latter are at an earlier stage in
337 nucleocapsid synthesis. Taken together, these subnanometer resolution map observations strongly
338 support the concept that CVSC occupancy can be used as an indicator for the progression of
339 herpesvirus capsid assembly *in situ* and identifies capsids with varying levels of residual scaffold
340 protein as CAIs along a continuum, having the potential for genome packaging rather than failed
341 assembly dead ends.

342 **Portal vertex architecture differences between CAIs and C-capsids.**

343 In contrast to previous high-resolution single particle cryo-EM structures of biochemically purified
344 herpesvirus capsids, the portal vertex for VZV capsids could not be reconstructed in previous
345 reports [39,41] but has been achieved by Cao et al [68]; this was not performed in infected cells *in situ*.
346 To address this issue, we developed a RELION pipeline to reconstruct the VZV unique portal

347 vertex, which was successfully identified for CAIs without the packaged dsDNA genome, or C-
348 capsids within a subset of cryo-FIB/ET tomograms using STA and 3D classification of capsid
349 vertices (**Fig. 6; Suppl. Fig. 16 to 18**). An initial cryo-ET map (23.6Å) for the unique portal vertex
350 revealed a density within the capsid cavity reminiscent of the herpesvirus portal [34,38,48-50], and an
351 absence of density for penton proteins compared to the 8.3Å cryo-ET map of the capsid vertex
352 (**Fig. 3 to 5; Suppl. Fig. 17a**). Further STA of the portal density generated a 22.9Å cryo-ET map
353 of the VZV portal with C12 symmetry (**Suppl. Fig. 17b**). A molecular model based on an
354 AlphaFold prediction of an individual VZV portal protein (pORF54; 769aa) and modelling of 12
355 subunits based on the entire HSV-1 portal was placed into the 22.9Å cryo-ET map of the VZV
356 portal (**Suppl. Fig. 17c and 17d**). Additional densities in the portal cryo-ET map were attributed
357 to poor modelling by AlphaFold of amino acids 1 to 64 and 656 to 769, which were disordered
358 and removed from the model. Architectural differences between the portal vertices of CAIs and
359 C-capsids were visible when cryo-ET map reconstructions were performed based on capsid type
360 (**Fig 6; Suppl. Fig. 18**). The portal cap was absent for CAIs compared to C-capsids, which was
361 apparent when the entire capsid was reconstructed (**Suppl. Fig. 18**). The unique portal structure
362 of C-capsids was confirmed as the portal density in the capsid cavity was only present at a single
363 vertex (**Suppl. Fig. 18**). Further capsid-type specific architectural differences were evident from
364 portal vertex cryo-ET maps and fitment of the molecular models for the peripentonal hexons, Ta
365 and Tc triplexes, CVC1, ORF22 helices, and the portal (**Fig. 6**). As expected, densities for the
366 pentonal MCP and alpha helices for the CVSC were absent and a channel for dsDNA translocation
367 was visible through the center for the CAIs capsid portal vertex cryo-ET map (**Fig. 6b and 6c**). In
368 contrast, the C-capsid cryo-ET map had a portal cap with densities for the CVSC, and which filled
369 the portal vertex channel (**Fig 6e and 6f**), presumably, tentacle helices and the dsDNA genome
370 terminus as previously described for HSV-1 [38]. As expected from the VZV vertex focused
371 classification analysis (**Fig. 5g to 5i**), occupancy of the CVSC at the non-portal vertices of the CAI
372 was incomplete whereas each vertex for the C-capsid exhibited a full complement of the CVSC
373 (**Fig. 6a and 6d; Suppl. Fig. 16**). These findings further support the CVSC as a defining element
374 and thus a marker of herpesvirus capsid assembly and maturity inside the cell nucleus during
375 replication.

376 **DISCUSSION**

377 The cell nucleus is a complex, crowded, dynamic environment, raising many questions about how
378 herpesvirus capsids assemble within this large organelle. This study reveals the power of cryo-ET
379 for the *in situ* investigation of herpesvirus assembly and morphogenesis at subnanometer
380 resolution, the localization of macromolecular structures inside herpesvirus infected cell nuclei,
381 and the reconstruction and segmentation of individual capsid proteins, allowing the identification
382 of capsid assembly intermediates (CAIs) in their native environment for replication. In addition,
383 the observations of procapsid precursors and architectural differences in capsid vertices revealed
384 by the CVSC distribution on capsids in VZV infected cells provided new information relevant for
385 understanding the temporal nature of herpesvirus capsid assembly inside the cell nucleus.

386 Herpesviruses are thought to assemble in a similar fashion to dsDNA bacteriophages where the
387 capsomeres coalesce with the scaffold protein to generate procapsids [28,29]. The high-resolution
388 imaging inside the nucleus of VZV infected cells in the present study revealed angular segment
389 structures where capsomeres, formed by the MCP and SCP, were associated with electron dense
390 material presumed to be scaffold protein (**Suppl. Fig. 2**). This interpretation is supported by cell
391 free systems that recapitulate herpesvirus capsid assembly by expression of the MCP, TRX1,
392 TRX2 and VP22a proteins [83]. VP22a is the scaffold protein expressed from UL26.5 (VZV
393 ORF33.5) cleaved by the VP24 protease during maturation [84,85]. VP24 is a cleavage product
394 derived from UL26 (VZV ORF33), where the protease autocatalytically cleaves the UL26 gene
395 product into VP24 and VP21. VP24 protease activity triggers spherical procapsids to undergo
396 angularization and the SCP (VP26) is thought to provide additional capsid stability [33,86-88]. For
397 VZV, the ORF33 protease is required for replication and a SCP (ORF23) null virus produces
398 predominantly spherical capsids, replicates poorly in cell culture and is non-viable in human skin
399 xenografts [89,90]. Furthermore, previous transient transfection studies have shown that the scaffold
400 protein is required for intranuclear localization of the HSV-1 MCP (VP5) [91] whereas nuclear
401 translocation of the VZV MCP is impaired by deleting the SCP [90]. Further characterization of
402 HSV procapsid formation in cell free expression systems noted the fragility and production of
403 angular segments, leading to a proposed model where capsomeres and scaffold protein aggregate
404 to form angular segments which in turn form spherical procapsids [92]. In support of this, the angular
405 segment structures of VZV demonstrate that herpesvirus procapsids form within the nucleus

406 through cooperative assembly of capsomere-associated scaffold protein subunits rather than
407 directly on a spherical precursor structure that recruits individual capsomeres.

408 Our study demonstrates that the acquisition of high-resolution 3D structure information derived
409 from vitrified cells is critical for differentiating between capsid types that occur during assembly.
410 Empty capsids were not apparent in the infected cell nucleus whereas previous observations with
411 traditional thin section EM of infected cell nuclei frequently identify capsid cavities devoid of
412 protein and dsDNA [30], leading to their conventional classification as A-capsids. From our 3D
413 observations, evidence of scaffold remnants inside the capsid cavity were lost when the 2D
414 sectional plane spans the entire diameter of the capsid, leading to their potential
415 mischaracterization. Furthermore, our data eliminate fixation, sectioning, and staining artefacts,
416 which could also lead to mischaracterization of A-capsids. In addition, capsid purification
417 methods can produce empty capsids as an artefact since the pressurized dsDNA genome can be
418 ejected due to the instability of the CVSC at the portal vertex [32]. In contrast, the 3D analyses of
419 capsid architecture coupled with the binding of CVSC heteropentamers to icosahedral vertices in
420 the infected cell points to the need for an amended classification. In the present study, capsids
421 with packaged dsDNA had the highest level of CVSC occupancy, consistent with previous single
422 particle cryo-EM of purified C-capsids [33,37,40,42,47] and, furthermore, assembly intermediates were
423 identifiable by correlating CVSC occupancy with levels of residual scaffold protein. Increasing
424 CVSC occupancy at the vertices and of heteropentamer copies (up to the maximum of five) was
425 associated with diminished quantities of scaffold protein in the capsid cavity. These observations
426 indicate that conventionally designated B-capsids represent a continuum of CAIs that can
427 potentially progress towards DNA encapsidation and formation of mature capsids ready for
428 nuclear egress.

429 Earlier high-resolution cryo-EM studies of VZV capsids were not able to visualize the unique
430 portal vertex [39,41]. However, a recent study reconstructed the portal vertex from purified capsids
431 [68]. In the present *in situ* study, reconstruction of the portal vertex for CAIs and C-capsids along
432 with acquisition of the VZV portal cap and packaged DNA for C-capsids was performed with
433 capsids inside the infected cell nucleus. The dodecameric portal for VZV is composed of pORF54,
434 which is essential for the packaging and cleavage of the dsDNA genome[93,94]. Similar to the VZV
435 cryo-ET maps of the unique portal vertex in the present study, cryo-EM studies of purified HSV,
436 HCMV, KSHV, and EBV have described the molecular architecture of the portal and portal vertex

437 to have a C12 to C5 symmetry mismatch of the portal and vertex constituents [34,35,38,49]. For HSV,
438 the CVSC is visible at the portal vertex and the CVC2 protein is required for dsDNA packaging
439 [38]. The CVC1 subunit sits atop the Ta and Tc triplexes. At the portal, for HSV-1, the Ta triplexes
440 are rotated 120° anticlockwise about their respective centers compared to pentonal Ta triplexes [38].
441 Thus, the triplexes and the CVC1 are at an altered angle compared to the other 11 vertices. The
442 MCP of HSV in the peripentonal hexon at position 6 has spine helices that extend into the pentonal
443 space at non-portal vertices [38]. The extension of the N-terminal helix was not visible in previous
444 VZV cryo-EM structures, and that absence can now be attributed to the loss of 'signal' due to the
445 combined STA of the portal and non-portal vertices [39,41]. Moreover, the head groups of the CVC2
446 dimer, important for dsDNA genome packaging and retention, form part of the portal cap, which
447 was not observed in previous studies of VZV, and explains the role of the CVSC in capsid
448 maturation.

449 In addition to the retention of the dsDNA genome, the CVSC has also been linked to nuclear
450 egress, a critical mechanism enabling capsids to leave the nucleus and enter the cytoplasm to
451 complete herpesvirus morphogenesis [95,96]. The process of nuclear egress is thought to be initiated
452 by capsids budding at the nuclear envelope into the perinuclear space through interactions of
453 CVC2 head groups with the nuclear egress complex (NEC) embedded in the INM, leading to
454 acquisition of a primary envelope [95,97]. Although the NEC has been shown to induce curvature in
455 the absence of CVC2 via a mechanism that involves a random lattice formation [98], these studies
456 were performed using a US3 mutant that causes capsids to become trapped within the perinuclear
457 space [99]. It has also been proposed that the CVSC functions as a selective switch to preferentially
458 allow the dsDNA genome-filled C-capsids to leave the nucleus [45,96]. Previous studies of capsid
459 structures at subnanometer or near atomic resolution were performed with capsids purified from
460 the nuclei of infected cells or purified herpesvirus particles, providing conflicting information
461 about the quantities of the CVSC associated with capsid vertices [33,36-41,47]. For VZV, precise
462 information about the occupancy of the CVSC was unknown, likely due to the purification of these
463 particles by ultracentrifugation and detergent-based removal of the envelope and tegument from
464 C-capsids [39,41]. Purification approaches have limitations in defining the stages of acquisition of
465 the CVSC on capsids. However, the extensive interactions among all five subunits of the
466 heteropentamer imply that the CVSC components co-assemble in the nucleus and act together as
467 a functional unit in binding the capsid vertices [33]. The present study provides definitive proof that

468 the CVSC can assemble as a heteropentamer and bind to capsids inside the nuclei of VZV infected
469 cells. Moreover, the application of STA and focused classification to the capsids further enabled
470 the determination of the CVSC occupancy at individual sites at the vertices in relationship to
471 different capsid types, supporting the notion that capsids with variable levels of scaffold protein
472 are intermediates. Studies of HCMV support this concept, as the frequency of morphologically
473 defined A-capsids within infected cell nuclei was very low compared to B- and C-capsids [31,32] and
474 C-capsids purified from infected cell nuclei ejected their genomes leading to higher quantities of
475 apparent A-capsids compared to those seen by TEM [32]. Furthermore, the A-capsids were covered
476 with the HCMV tegument protein pp150, which is equivalent to the CVSC of alphaherpesviruses
477 and typically associated with C-capsids [32,42,100]. Thus, high-resolution imaging coupled with state-
478 of-the-art image classification approaches can now assign temporal information to the dynamic
479 herpesvirus capsid assembly process *in situ*. The near complete occupancy of the CVSC on C-
480 capsids and the increased levels of the CVSC on capsids with limited scaffold protein further
481 support a selective function of the CVSC for nuclear egress, as both of these capsid types are found
482 in extracellular VZV particles.

483 Our study provides direct evidence that the CVSC has a critical role in herpesvirus capsid assembly
484 within the host cell nucleus, revealing heterogeneity in CVSC occupancy associated with CAIs,
485 with the highest frequency found on dsDNA genome-filled C-capsids. Rather than discrete A-, B-
486 , and C-capsid categories, we propose a model of herpesvirus capsid assembly where CVSC
487 acquisition serves as a temporal marker towards completion; CAIs progress along a continuum
488 defined by decreasing scaffold protein and increasing CVSC occupancy prior to genome
489 packaging. Early intermediates retain abundant scaffold and have few CVSCs, whereas later
490 intermediates contain limited scaffold with more extensive CVSC occupancy at the vertices,
491 culminating in C-capsids with full vertex occupancy and packaged genomes. This model
492 integrates structural heterogeneity into a dynamic pathway, resolves the ambiguity surrounding A-
493 and B-capsids, and highlights CVSC acquisition as a critical determinant of capsid stability,
494 genome retention, and readiness for nuclear egress. Our observations shed light on the unresolved
495 question about whether A- and B-capsids are assembly dead ends, instead suggesting that A-
496 capsids represent artefacts from purification whereas those conventionally grouped as B-capsids
497 are assembly intermediates that can be further differentiated based on CVSC occupancy. Our
498 findings underscore the intricate and dynamic nature of capsid assembly *in situ* during herpesvirus

499 replication, providing new insights for the development of novel therapeutic strategies targeting
500 herpesvirus capsid maturation.

501

502 **MATERIALS and METHODS**

503 **Reagents, consumables, and resources.** All reagents, consumables, and resources, including
504 supplier information where applicable, are provided in **Suppl. Table 5**.

505 **Cells lines.** MeWo cells (HTB-65; ATCC) were propagated in minimal essential medium
506 (Corning Cellgro) supplemented with 10% fetal bovine serum (FBS; Invitrogen), nonessential
507 amino acids (100 µM; Corning Cellgro), antibiotics (penicillin, 100 U/ml; streptomycin, 100
508 µg/ml; Invitrogen) and the antifungal agent amphotericin B (250 µg/ml; Invitrogen) at 37°C in a
509 humidified atmosphere with 5% CO_2.

510 **Viruses.** The VZV parental Oka strain was originally cloned into a bacterial artificial chromosome
511 (BAC) and designated pPOKA-BAC-DX [101]. Recombinant viruses pOka-TK-GFP (pOka-rTK)
512 and pOka-TK-RFP were generated in a previous study [71,102].

513 **ECM micropatterning of SiO_2 EM grids.** To position MeWo cells centrally within EM grid
514 squares, 300 mesh gold grids coated with a thin perforated layer of SiO_2 (Quantifoil R2/2) were
515 subjected to micropatterning following the procedure available at protocols.io
516 (https://www.protocols.io/view/micropatterning-em-grids-for-cryo-electron-tomogra-
517 rm7vz3wqrgx1/v1). Briefly, EM grids were exposed to atmospheric plasma, incubated in poly-L-
518 lysine (0.01%; Sigma) and subsequent incubations with 0.1M HEPES + mPEGSuccinimidyl
519 Valerate (PEG-SVA MW 5,000; 100 mg/ml; Laysan Bio Inc.) then PLPP gel (1:6 dilution in H_2O;
520 Alveole). The coated grids were exposed to UV light according to a digitally generated
521 micropattern (30x30µm or 33x33µm to match the 300 mesh spacing) that covered the EM grid
522 square using a Primo photo-micropatterning system (Alveole) to selectively degrade the PEG
523 coating to remove the hydrophobic antifouling layer. An extracellular matrix (ECM) surrogate,
524 Gelatin Oregon Green 488 (1 mg/ml; Invitrogen), was applied to the grids prior to cell seeding.

525 **Vitrification of VZV Infected MeWo cells on ECM micropatterned grids.** Cell free VZV
526 cannot be purified to high titers making direct infection of cells grown on EM grids with high
527 MOIs needed for productive infection impractical. Thus, infected cells were seeded directly onto

528 ECM micropatterned EM grids. VZV (pOKA-TK-RFP) infected MeWo cells were passaged onto
529 freshly seeded uninfected MeWo cells 24 hours prior to the day of seeding. On the day of seeding,
530 the VZV infected MeWo cells were then passaged onto uninfected MeWo cells and incubated for
531 8 hours. The infected cells were then trypsinized, centrifuged at 400RCF for 5 minutes then
532 resuspended in maintenance media to yield one cell per grid square; determined empirically on the
533 day of seeding. Infected and uninfected cell suspensions were applied to the ECM micropatterned
534 grids in 35mm glass bottomed dishes (MatTech P35G-1.5-14-C). After 2 hours incubation at 37°C
535 in a humidified atmosphere with 5% CO_2, 3 ml of maintenance media was added and incubated
536 for an additional 16 hours. Grids were removed from the maintenance media and plunge frozen
537 into liquid ethane using an EM GP2 (Leica) with humidity at 99% and a blot time of 9 seconds.

538 **Cryo-FIB/SEM of vitrified VZV infected MeWo cells.** An Aquilos 2 cryo-FIB/SEM
539 microscope (ThermoFisher) was used to generate lamella from VZV infected cells on
540 micropatterned grids. Prior to milling, the grids were platinum coated. Microexpansion joints of
541 1µm width and 4µm between the milled area and the microexpansion joint were used to relieve
542 tension on the final lamellae[103]. The primary milling step was performed at 1nA and 5µm height
543 and 15µm width with two 1µm microexpansion joints milled either side at 4 µm from the lamella
544 milling site. Successive milling steps of 3µm (300pA), 1µm (100pA), 500nm (50pA), and a final
545 polishing step of 175nm (30pA) were performed to generate lamella with a target thickness of
546 175nm. Lamella were produced for 6 to 10 cells per grid.

547 **Cryo-ET of whole or cryo-FIB/SEM milled VZV infected MeWo cells.** Tilt series were either
548 collected at the periphery of whole vitrified VZV infected MeWo cells on EM grids, using a 200kV
549 Talos Arctica (FEI) or at cryo-FIB/SEM generated lamella, using a 300kV Titan Krios (FEI)
550 controlled by SerialEM [104] to automate the data collection procedure using the parameters outlined
551 in **Suppl. Table 1**. To identify areas of interest for tilt series collection, medium magnification
552 (4,800-11,500x) montages were generated, and imaging sites were determined empirically by eye.
553 Due to the large size of herpesvirus capsids, a 3.44Å/pixel size was chosen to accommodate areas
554 where high frequencies of VZV capsids were present in the nucleus. A total of 399 tilt series were
555 collected from cryo-FIB/SEM milled lamella across five, 3-day sessions on 300kV Titan Krios
556 microscopes. A total of 194 tomograms were generated for VZV capsid quantification, analysis,
557 and cryo-ET map reconstructions.

558 **Cryo-ET image processing.** Motion correction, damage compensation, CTF estimation, and tilt
559 series generation was performed using Warp [105]. Tomogram reconstruction for visualization was
560 performed using the IMOD tomography GUI Etomo [106]. Tomogram processing and associated
561 movie files were generated using 3dmod [107]. Segmentation of tomograms was performed using
562 Dragonfly software (Version 2022.2 for [Windows]. Comet Technologies Canada Inc., Montreal,
563 Canada; software available at https://www.theobjects.com/dragonfly). Movies were generated
564 using FFmpeg (FFmpeg Developers. (2016). ffmpeg tool (Version be1d324) available from
565 http://ffmpeg.org/).

566 **Subnanometer resolution cryo-ET map reconstruction of the VZV capsid vertex.** To
567 reconstruct the VZV capsid vertex and 3-fold axis of symmetry a WARP-EMAN2 data processing
568 strategy was used (**Suppl. Fig. 11**). Tilt series generated by WARP were imported into EMAN2
569 for tomogram alignment using patch tracking where handedness was checked and CTF measured.
570 The convolutional neural network was employed to select particles (box size 512; n=1,084 capsids)
571 from 194 tomograms and make sets (bin2). An initial model was generated from the sets using
572 e2spt_sgd_new.py (--res=50.0; --niter=30; --shrink=4; --sym=icos) followed by subtomogram-
573 subtilt refinement using e2spt_refine_new.py (--startres=30.0; --sym=icos; --iters=p3,t2,p,t,r,d; --
574 keep=0.95; --tophat localwiener –goldstandard). Classification with icosahedral symmetry was
575 performed on the output to remove poor quality particles that can negatively influence the
576 subtomogram averaging; e2spt_refinemulti_new.py (--nref 3; --maxres 40; --loadali3d; --skipali;
577 --sym icos; --maskalign spt_01/mask.hdf; --niter 20). Further refinement of 317 capsids produced
578 a cryo-ET map of the entire VZV capsids of 13.0Å resolution. To generate a subnanometer
579 resolution cryo-ET map for the VZV capsid vertex, symmetry expansion was performed with the
580 317 capsids using e2spt_extract.py (--postxf icos,0,0,110; --compressbits 8; --boxsz_unbin 192; -
581 -newlabel pent2; --mindist 500; --loadali2d) followed by building sets; e2spt_buildsets.py (--
582 label=pent2; --allparticles; --spliteo). An average of the extracted particles was generated from
583 the set using e2proc3d.py (--average; --averager mean.tomo; --avg_byxf). The average was then
584 refined using e2spt_refine_new.py (--startres=30.0; --sym=c5; --iters=p3,t2,p,t,r,d; --
585 keep=0.8,0.95,0.95; --tophat localwiener; --localrefine; --goldstandard) to achieve a cryo-ET map
586 of the VZV capsid vertex at 8.3Å resolution. A similar procedure was used for the 3-fold axis of
587 symmetry to achieve a cryo-ET map at 8.4Å resolution.

588 **Segmentation of the 3-fold and 5-fold cryo-ET maps.** The 3- and 5-fold cryo-ET maps of the
589 VZV capsid were segmented based on the 7BW6 asymmetric unit model of the VZV A-capsid [39]
590 using ChimeraX [108]. To segment the CVSC density in the 5-fold axis cryo-ET map, AlphaFold 2
591 [109] was used to model the heteropentamer based on the full-length proteins CVC1 (ORF43;
592 monomer) and CVC2 (ORF34; dimer), and 45 C-terminal amino acids (2724-2768) of VP1/2
593 (ORF22). Molecular dynamics flexible fitting (MDFF) was performed to fit the two head groups
594 of the CVC2 dimer into the cryo-ET map using NAMD [110] following the procedure outlined in the
595 VMD tutorial. Conversion of the cryo-EM map to an MDFF potential, rigid body docking of the
596 CVSC, initial structure generation, and secondary structure restraint definitions were all performed
597 using VMD. The output files were used as input to run NAMD with the following parameters;
598 step 1 -gscale 0.3, -numsteps 50000; step 2 -gscale 10, -numsteps 100000. A model of the
599 asymmetric unit of the VZV capsid vertex, including the CVSC, was refined using ISOLDE [111].
600 All images and movie files were generated using ChimeraX. Movies were generated using
601 FFmpeg.

602 **Three axis orthogonal projection and uniform manifold approximation projection.** The 3D
603 VZV capsid particles were aligned to the symmetrized capsid reference from the EMAN2
604 icosahedral refinement. The subsequent 2D sub-tilt particles at the corresponding orientation were
605 reconstructed with icosahedral symmetry to obtain symmetrized 3D particles free from missing
606 wedge artifacts. Each particle was projected along three orthogonal axes of thin central slabs
607 (72Å), using only one quarter of the volume closest to the center perpendicular to the
608 corresponding axis. The resulting three 2D image projections per capsid were stacked and
609 flattened into a 1D array that was used as input for uniform manifold approximation projection
610 (UMAP). After manifold embedding, particles on the 2D UMAP space were clustered using a K-
611 means algorithm to produce the individual classes.

612 **Reconstruction of the VZV Portal Vertex.** To reconstruct the VZV portal vertex a WARP-
613 IMOD-EMAN2-Relion data processing strategy was used (**Suppl. Fig. 16**). Tilt series were
614 aligned using IMOD and for the final aligned stack, unbinned, CTF estimation was performed
615 using CTFplotter with the 'Find astigmatism option' checked. Tomograms for Relion were
616 generated using relion_tomo_reconstruct_tomogram and used for particle picking of capsids in
617 EMAN2 (n=471). Tomograms and particle coordinates were imported into Relion using Tomo
618 Import. Make pseudo-subtomos was used to make subtomograms (bin 4; 13.76 Å/pixel) using a

619 box size (pixels) of 360 and cropped box size (pixels) of 180. An initial model was generated
620 using 3D initial model and a mask was generated using Dynamo and Mask create. A 3D refinement
621 was performed with 3D auto-refine with an initial low-pass filter of 50 Å and I3 symmetry. Particle
622 reconstruction was performed (bin2; 6.88Å/pixel) with Tomo reconstruct particle with a box size
623 of 440 and cropped box size of 220 with I3 symmetry, which was used to generate a new mask,
624 followed by reconstruction of subtomograms using Make pseudo-subtomos. A 3D refinement was
625 performed with 3D auto-refine with an initial low-pass filter of 30Å and I3 symmetry. The output
626 was used for Tomo frame alignment, particle reconstruction (bin 1; 3.44Å/pixel; box size 440
627 pixels; I3 symmetry), mask creation, reconstruction of subtomograms, and 3D refinement with an
628 initial low-pass filter of 14Å and I3 symmetry, generating a 12.1Å cryo-ET map of the VZV
629 capsid.

630 Symmetry expansion was performed using relion_particle_symmetry_expand with --sym I3. This
631 process produces 5 rotations per vertex; redundant _rlnAngleRot values were removed to leave 12
632 unique vertices per capsid (n=5,652). Vertices beyond the boundaries of the tomograms were
633 removed (n=5,318). The Z height was adjusted to center the vertices in the center of the box using
634 relion_star_handler and --center_Z command. The output was used for particle reconstruction (bin
635 4; 13.76 Å/pixel; initial box size 120 pixels; cropped box size 60 pixels; C5 symmetry), mask
636 creation, reconstruction of subtomograms, and 3D refinement with an initial low-pass filter of 50Å
637 and C5 symmetry. The output was used for particle reconstruction (bin 2; 6.88 Å/pixel; box size
638 240 pixels; cropped box size 120 pixels; C5 symmetry), mask creation, reconstruction of
639 subtomograms, and 3D refinement with an initial low-pass filter of 30Å and C5 symmetry. The
640 output was used for particle reconstruction (bin 1; 3.44Å/pixel; box size 240 pixels; C5 symmetry),
641 mask creation, reconstruction of subtomograms, and 3D refinement with an initial low-pass filter
642 of 15Å and C5 symmetry, generating a 10.3Å cryo-ET map of the VZV capsid vertex.

643 The output was used to generate a cryo-ET capsid vertex map at bin 4 using the above processing
644 scheme then used to perform 3D classification (12 classes; 29 iterations). An initial 60 particles
645 were selected based on the presence of a portal density and the absence of the pentonal major
646 capsid protein then used to generate a cryo-ET portal vertex map at bin 4 using the above
647 processing scheme. A focused cylindrical mask was generated and used for further 3D
648 classification of the VZV capsid vertices yielding a total of 103 portal vertices. A final round of
649 template-based 3D classification yielded a total of 109 portal vertices. The output was used for

650 particle reconstruction (bin 2; 6.88Å/pixel; box size 240 pixels; cropped box size 120 pixels; C5
651 symmetry), mask creation, reconstruction of subtomograms, and 3D refinement with an initial
652 low-pass filter of 30Å and C5 symmetry, generating a 23.6Å cryo-ET map of the VZV capsid
653 portal vertex. To reconstruct the portal, particle reconstruction (bin 2; 6.88Å/pixel; box size 90
654 pixels; cropped box size 30 pixels; C12 symmetry), mask creation, reconstruction of
655 subtomograms, and 3D refinement with an initial low-pass filter of 30Å, C12 symmetry, and C1
656 symmetry relaxation was performed, generating a 22.9Å cryo-ET map of the VZV portal.

657 To identify portal vertex specific features, the 109 portal vertices were divided into CAI (n=62)
658 and C-capsids (n=47) based on morphological features; either scaffold protein (CAI) or genomic
659 DNA (C-capsids) inside the capsid cavity. Cryo-ET maps for the portal vertices from CAI (23.8Å)
660 and C-capsids (24.3Å) were generated as described above; particle reconstruction (bin 2;
661 6.88Å/pixel; box size 240 pixels; cropped box size 120 pixels; C5 symmetry), mask creation,
662 reconstruction of subtomograms, and 3D refinement with an initial low-pass filter of 30Å and C5
663 symmetry. Cryo-ET maps for the entire capsid from CAI (32.6Å) and C-capsids (33.6Å) were
664 generated by first adjusting the Z-height of the particles as previously described the performing
665 particle reconstruction (bin 2; 6.88Å/pixel; box size 512 pixels; cropped box size 256 pixels; I3
666 symmetry), mask creation, reconstruction of subtomograms, and 3D refinement with an initial
667 low-pass filter of 30Å, C5 symmetry, and C1 symmetry relaxation.

668 The resolution of all Relion generated cryo-ET maps were confirmed using post-processing with
669 soft masks and assessed by Fourier Shell correlation curves with a cut-off at 0.143 from two
670 independent half-sets of the pseudosubtomograms.

671 **Statistics and Reproducibility.** All quantitative data were analyzed with two-way ANOVA to
672 determine statistical significance using Prism (GraphPad Software).

673 **DATA AVAILABILITY**

674 Data generated and/or analyzed during the current study are available in the paper, appended as
675 supplementary data, available in public repositories. The original cryo-ET movie files, tilt series,
676 and tomograms have been deposited in the Electron Microscopy Public Image Archive (EMPIAR)
677 with accession code EMPIAR-12464. The cryo-ET maps have been deposited in the Electron
678 Microscopy Data Bank (EMDB) with accession codes EMD-49591 for the vertex cryo-ET map
679 (model PDB 9NO1), EMD-49886 for the 3-fold axis cryo-ET map and EMD-49465 to 49473 for

680 cryo-ET maps of the portal vertex. The source data underlying Figures 5A, 5E, and 5I are provided
681 in the associated Source Data file.

682 **REFERENCES**

683 1 Arvin, A. M. & Abendroth, A. in *Fields Virology: DNA Viruses, 7e* (eds Peter M. Howley,
684 David M. Knipe, Blossom A. Damania, & Jeffrey I. Cohen) 0 (Lippincott Williams &
685 Wilkins, a Wolters Kluwer business, 2022).
686 2 Damania, B. & Cesarman, E. in *Fields Virology: DNA Viruses, 7e* (eds Peter M. Howley,
687 David M. Knipe, Blossom A. Damania, & Jeffrey I. Cohen) 0 (Lippincott Williams &
688 Wilkins, a Wolters Kluwer business, 2022).
689 3 Gewurz, B. E., Longnecker, R. M. & Cohen, J. I. in *Fields Virology: DNA Viruses, 7e* (eds
690 Peter M. Howley, David M. Knipe, Blossom A. Damania, & Jeffrey I. Cohen) 0
691 (Lippincott Williams & Wilkins, a Wolters Kluwer business, 2022).
692 4 Goodrum, F., Britt, W. & Mocarski, E. S. in *Fields Virology: DNA Viruses, 7e* (eds Peter
693 M. Howley, David M. Knipe, Blossom A. Damania, & Jeffrey I. Cohen) 0 (Lippincott
694 Williams & Wilkins, a Wolters Kluwer business, 2022).
695 5 Knipe, D. M., Heldwein, E. E., Mohr, I. J. & Sodroski, C. N. in *Fields Virology: DNA*
696 *Viruses, 7e* (eds Peter M. Howley, David M. Knipe, Blossom A. Damania, & Jeffrey I.
697 Cohen) 0 (Lippincott Williams & Wilkins, a Wolters Kluwer business, 2022).
698 6 Krug, L. T. & Pellett, P. E. in *Fields Virology: DNA Viruses, 7e* (eds Peter M. Howley,
699 David M. Knipe, Blossom A. Damania, & Jeffrey I. Cohen) 0 (Lippincott Williams &
700 Wilkins, a Wolters Kluwer business, 2022).
701 7 Mori, Y., Zerr, D. M., Flamand, L. & Pellett, P. E. in *Fields Virology: DNA Viruses, 7e*
702 (eds Peter M. Howley, David M. Knipe, Blossom A. Damania, & Jeffrey I. Cohen) 0
703 (Lippincott Williams & Wilkins, a Wolters Kluwer business, 2022).
704 8 Whitley, R. J. & Johnston, C. in *Fields Virology: DNA Viruses, 7e* (eds Peter M. Howley,
705 David M. Knipe, Blossom A. Damania, & Jeffrey I. Cohen) 0 (Lippincott Williams &
706 Wilkins, a Wolters Kluwer business, 2022).
707 9 Gilden, D. H., Mahalingham, R., Deitch, S. & Randall, C., J. in *Alpha herpesviruses :*
708 *molecular and cellular biology* (ed R. M. Sandri-Goldin) 402 (Caister Academic, 2006).

709 10 Banovic, T. *et al.* Disseminated varicella infection caused by varicella vaccine strain in a
710 child with low invariant natural killer T cells and diminished CD1d expression. *J Infect*
711 *Dis* **204**, 1893-1901, (2011).
712 11 Gilden, D., Cohrs, R. J., Mahalingam, R. & Nagel, M. A. Varicella zoster virus
713 vasculopathies: diverse clinical manifestations, laboratory features, pathogenesis, and
714 treatment. *Lancet Neurol* **8**, 731-740, (2009).
715 12 Jean-Philippe, P. *et al.* Severe varicella caused by varicella-vaccine strain in a child with
716 significant T-cell dysfunction. *Pediatrics* **120**, e1345-1349, (2007).
717 13 Johnson, R. W. Zoster-associated pain: what is known, who is at risk and how can it be
718 managed? *Herpes* **14 Suppl 2**, 30-34, (2007).
719 14 Pahud, B. A., Glaser, C. A., Dekker, C. L., Arvin, A. M. & Schmid, D. S. Varicella zoster
720 disease of the central nervous system: epidemiological, clinical, and laboratory features 10
721 years after the introduction of the varicella vaccine. *J Infect Dis* **203**, 316-323, (2011).
722 15 Schmader, K. Herpes zoster and postherpetic neuralgia in older adults. *Clin Geriatr Med*
723 **23**, 615-632, vii-viii, (2007).
724 16 Brunell, P. A., Geiser, C. F., Novelli, V., Lipton, S. & Narkewicz, S. Varicella-like illness
725 caused by live varicella vaccine in children with acute lymphocytic leukemia. *Pediatrics*
726 **79**, 922-927, (1987).
727 17 Marin, M., Meissner, H. C. & Seward, J. F. Varicella prevention in the United States: a
728 review of successes and challenges. *Pediatrics* **122**, e744-751, (2008).
729 18 Pickering, L. K. *et al.* Immunization programs for infants, children, adolescents, and adults:
730 clinical practice guidelines by the Infectious Diseases Society of America. *Clin Infect Dis*
731 **49**, 817-840, (2009).
732 19 Han, J. Y., Hanson, D. C. & Way, S. S. Herpes zoster and meningitis due to reactivation
733 of varicella vaccine virus in an immunocompetent child. *Pediatr Infect Dis J* **30**, 266-268,
734 (2011).
735 20 Krause, P. R. & Klinman, D. M. Varicella vaccination: evidence for frequent reactivation
736 of the vaccine strain in healthy children. *Nat Med* **6**, 451-454, (2000).
737 21 Whitley, R. J. Therapy of herpes virus infections in children. *Adv Exp Med Biol* **609**, 216-
738 232, (2008).

739 22 Whitley, R. J., Volpi, A., McKendrick, M., Wijck, A. & Oaklander, A. L. Management of
740 herpes zoster and post-herpetic neuralgia now and in the future. *J Clin Virol* **48 Suppl 1**,
741 S20-28, (2010).
742 23 Shiraki, K., Takemoto, M. & Daikoku, T. Emergence of varicella-zoster virus resistance to
743 acyclovir: epidemiology, prevention, and treatment. *Expert Rev Anti Infect Ther* **19**, 1415-
744 1425, (2021).
745 24 Topalis, D., Gillemot, S., Snoeck, R. & Andrei, G. Thymidine kinase and protein kinase in
746 drug-resistant herpesviruses: Heads of a Lernaean Hydra. *Drug Resist Updat* **37**, 1-16,
747 (2018).
748 25 Harfouche, M. *et al.* Estimated global and regional incidence and prevalence of herpes
749 simplex virus infections and genital ulcer disease in 2020: mathematical modelling
750 analyses. *Sex Transm Infect*, (2024).
751 26 Chaiyakunapruk, N. *et al.* Estimated global and regional economic burden of genital herpes
752 simplex virus infection among 15-49 year-olds in 2016. *BMC Glob Public Health* **2**, 42,
753 (2024).
754 27 Davison, A. J. in *Human Herpesviruses: Biology, Therapy, and Immunoprophylaxis* (eds
755 A. Arvin *et al.*) (2007).
756 28 Baines, J. D. Herpes simplex virus capsid assembly and DNA packaging: a present and
757 future antiviral drug target. *Trends Microbiol* **19**, 606-613, (2011).
758 29 Heming, J. D., Conway, J. F. & Homa, F. L. Herpesvirus Capsid Assembly and DNA
759 Packaging. *Adv Anat Embryol Cell Biol* **223**, 119-142, (2017).
760 30 Gibson, W. & Roizman, B. Proteins specified by herpes simplex virus. 8. Characterization
761 and composition of multiple capsid forms of subtypes 1 and 2. *J Virol* **10**, 1044-1052,
762 (1972).
763 31 Tandon, R., Mocarski, E. S. & Conway, J. F. The A, B, Cs of herpesvirus capsids. *Viruses*
764 **7**, 899-914, (2015).
765 32 Stevens, A., Cruz-Cosme, R., Armstrong, N., Tang, Q. & Zhou, Z. H. Structure-guided
766 mutagenesis targeting interactions between pp150 tegument protein and small capsid
767 protein identify five lethal and two live-attenuated HCMV mutants. *Virology* **596**, 110115,
768 (2024).

769 33 Dai, X. & Zhou, Z. H. Structure of the herpes simplex virus 1 capsid with associated
770 tegument protein complexes. *Science* **360**, (2018).
771 34 Gong, D. *et al.* DNA-Packing Portal and Capsid-Associated Tegument Complexes in the
772 Tumor Herpesvirus KSHV. *Cell* **178**, 1329-1343 e1312, (2019).
773 35 Li, Z., Pang, J., Dong, L. & Yu, X. Structural basis for genome packaging, retention, and
774 ejection in human cytomegalovirus. *Nat Commun* **12**, 4538, (2021).
775 36 Li, Z. *et al.* CryoEM structure of the tegumented capsid of Epstein-Barr virus. *Cell Res* **30**,
776 873-884, (2020).
777 37 Liu, W. *et al.* Structures of capsid and capsid-associated tegument complex inside the
778 Epstein-Barr virus. *Nat Microbiol* **5**, 1285-1298, (2020).
779 38 Liu, Y. T., Jih, J., Dai, X., Bi, G. Q. & Zhou, Z. H. Cryo-EM structures of herpes simplex
780 virus type 1 portal vertex and packaged genome. *Nature* **570**, 257-261, (2019).
781 39 Sun, J. *et al.* Cryo-EM structure of the varicella-zoster virus A-capsid. *Nat Commun* **11**,
782 4795, (2020).
783 40 Wang, G. *et al.* Structures of pseudorabies virus capsids. *Nat Commun* **13**, 1533, (2022).
784 41 Wang, W. *et al.* Near-atomic cryo-electron microscopy structures of varicella-zoster virus
785 capsids. *Nat Microbiol* **5**, 1542-1552, (2020).
786 42 Yu, X., Jih, J., Jiang, J. & Zhou, Z. H. Atomic structure of the human cytomegalovirus
787 capsid with its securing tegument layer of pp150. *Science* **356**, (2017).
788 43 Zhang, Y. *et al.* Atomic structure of the human herpesvirus 6B capsid and capsid-
789 associated tegument complexes. *Nat Commun* **10**, 5346, (2019).
790 44 Dai, X. *et al.* Structure and mutagenesis reveal essential capsid protein interactions for
791 KSHV replication. *Nature* **553**, 521-525, (2018).
792 45 Huet, A., Huffman, J. B., Conway, J. F. & Homa, F. L. Role of the Herpes Simplex Virus
793 CVSC Proteins at the Capsid Portal Vertex. *J Virol* **94**, (2020).
794 46 Sae-Ueng, U. *et al.* Major capsid reinforcement by a minor protein in herpesviruses and
795 phage. *Nucleic Acids Res* **42**, 9096-9107, (2014).
796 47 Wang, J. *et al.* Structure of the herpes simplex virus type 2 C-capsid with capsid-vertex-
797 specific component. *Nat Commun* **9**, 3668, (2018).
798 48 Li, Z. *et al.* Cryo-electron microscopy structures of capsids and in situ portals of DNA-
799 devoid capsids of human cytomegalovirus. *Nat Commun* **14**, 2025, (2023).

800 49 Machon, C. *et al.* Atomic structure of the Epstein-Barr virus portal. *Nat Commun* **10**, 3891,
801 (2019).
802 50 Schmid, M. F. *et al.* A tail-like assembly at the portal vertex in intact herpes simplex type-
803 1 virions. *PLoS Pathog* **8**, e1002961, (2012).
804 51 Draganova, E. B., Valentin, J. & Heldwein, E. E. The Ins and Outs of Herpesviral Capsids:
805 Divergent Structures and Assembly Mechanisms across the Three Subfamilies. *Viruses* **13**,
806 (2021).
807 52 Diwaker, D. & Wilson, D. W. Microtubule-Dependent Trafficking of Alphaherpesviruses
808 in the Nervous System: The Ins and Outs. *Viruses* **11**, (2019).
809 53 Zaichick, S. V. *et al.* The herpesvirus VP1/2 protein is an effector of dynein-mediated
810 capsid transport and neuroinvasion. *Cell Host Microbe* **13**, 193-203, (2013).
811 54 Jih, J., Liu, Y. T., Liu, W. & Zhou, Z. H. The incredible bulk: Human cytomegalovirus
812 tegument architectures uncovered by AI-empowered cryo-EM. *Sci Adv* **10**, eadj1640,
813 (2024).
814 55 Buch, M. H. C., Newcomb, W. W., Winkler, D. C., Steven, A. C. & Heymann, J. B. Cryo-
815 Electron Tomography of the Herpesvirus Procapsid Reveals Interactions of the Portal with
816 the Scaffold and a Shift on Maturation. *mBio* **12**, (2021).
817 56 Cardone, G. *et al.* Visualization of the herpes simplex virus portal in situ by cryo-electron
818 tomography. *Virology* **361**, 426-434, (2007).
819 57 Dai, W. *et al.* Unique structures in a tumor herpesvirus revealed by cryo-electron
820 tomography and microscopy. *J Struct Biol* **161**, 428-438, (2008).
821 58 Deng, B., O'Connor, C. M., Kedes, D. H. & Zhou, Z. H. Direct visualization of the putative
822 portal in the Kaposi's sarcoma-associated herpesvirus capsid by cryoelectron tomography.
823 *J Virol* **81**, 3640-3644, (2007).
824 59 Deng, B., O'Connor, C. M., Kedes, D. H. & Zhou, Z. H. Cryo-electron tomography of
825 Kaposi's sarcoma-associated herpesvirus capsids reveals dynamic scaffolding structures
826 essential to capsid assembly and maturation. *J Struct Biol* **161**, 419-427, (2008).
827 60 Grunewald, K. *et al.* Three-dimensional structure of herpes simplex virus from cryo-
828 electron tomography. *Science* **302**, 1396-1398, (2003).
829 61 Newcomb, W. W. *et al.* The Primary Enveloped Virion of Herpes Simplex Virus 1: Its
830 Role in Nuclear Egress. *mBio* **8**, (2017).

831 62 Si, Z. *et al.* Different functional states of fusion protein gB revealed on human
832 cytomegalovirus by cryo electron tomography with Volta phase plate. *PLoS Pathog* **14**,
833 e1007452, (2018).
834 63 Chang, J. T., Schmid, M. F., Rixon, F. J. & Chiu, W. Electron cryotomography reveals the
835 portal in the herpesvirus capsid. *J Virol* **81**, 2065-2068, (2007).
836 64 Vijayakrishnan, S., McElwee, M., Loney, C., Rixon, F. & Bhella, D. In situ structure of
837 virus capsids within cell nuclei by correlative light and cryo-electron tomography. *Sci Rep*
838 **10**, 17596, (2020).
839 65 Bucks, M. A., O'Regan, K. J., Murphy, M. A., Wills, J. W. & Courtney, R. J. Herpes
840 simplex virus type 1 tegument proteins VP1/2 and UL37 are associated with intranuclear
841 capsids. *Virology* **361**, 316-324, (2007).
842 66 Fan, W. H. *et al.* The large tegument protein pUL36 is essential for formation of the capsid
843 vertex-specific component at the capsid-tegument interface of herpes simplex virus 1. *J*
844 *Virol* **89**, 1502-1511, (2015).
845 67 Schipke, J. *et al.* The C terminus of the large tegument protein pUL36 contains multiple
846 capsid binding sites that function differently during assembly and cell entry of herpes
847 simplex virus. *J Virol* **86**, 3682-3700, (2012).
848 68 Cao, L. *et al.* Insights into varicella-zoster virus assembly from the B- and C-capsid at near-
849 atomic resolution structures. *hLife* **2**, 64-74, (2024).
850 69 Reimer, L. & Kohl, H. *Transmission electron microscopy : physics of image formation*.
851 Fifth edition. edn, (Springer, 2008).
852 70 Schaffer, M. *et al.* A cryo-FIB lift-out technique enables molecular-resolution cryo-ET
853 within native Caenorhabditis elegans tissue. *Nat Methods* **16**, 757-762, (2019).
854 71 Oliver, S. L., Yang, E. & Arvin, A. M. Dysregulated Glycoprotein B-Mediated Cell-Cell
855 Fusion Disrupts Varicella-Zoster Virus and Host Gene Transcription during Infection. *J*
856 *Virol* **91**, (2017).
857 72 Oliver, S. L. *et al.* A glycoprotein B-neutralizing antibody structure at 2.8 A uncovers a
858 critical domain for herpesvirus fusion initiation. *Nat Commun* **11**, 4141, (2020).
859 73 Oliver, S. L. *et al.* The N-terminus of varicella-zoster virus glycoprotein B has a functional
860 role in fusion. *PLoS Pathog* **17**, e1008961, (2021).

861 74 Zhou, M., Kamarshi, V., Arvin, A. M. & Oliver, S. L. Calcineurin phosphatase activity
862 regulates Varicella-Zoster Virus induced cell-cell fusion. *PLoS Pathog* **16**, e1009022,
863 (2020).
864 75 Baker, M. L., Jiang, W., Rixon, F. J. & Chiu, W. Common ancestry of herpesviruses and
865 tailed DNA bacteriophages. *J Virol* **79**, 14967-14970, (2005).
866 76 Homa, F. L. *et al.* Structure of the pseudorabies virus capsid: comparison with herpes
867 simplex virus type 1 and differential binding of essential minor proteins. *J Mol Biol* **425**,
868 3415-3428, (2013).
869 77 DeRussy, B. M., Boland, M. T. & Tandon, R. Human Cytomegalovirus pUL93 Links
870 Nucleocapsid Maturation and Nuclear Egress. *J Virol* **90**, 7109-7117, (2016).
871 78 Evilevitch, A. & Sae-Ueng, U. Mechanical Capsid Maturation Facilitates the Resolution
872 of Conflicting Requirements for Herpesvirus Assembly. *J Virol* **96**, e0183121, (2022).
873 79 McInnes, L. & Healy, J. UMAP: Uniform Manifold Approximation and Projection for
874 Dimension Reduction. *ArXiv* **abs/1802.03426**, (2018).
875 80 Chen, M. & Ludtke, S. J. Deep learning-based mixed-dimensional Gaussian mixture model
876 for characterizing variability in cryo-EM. *Nat Methods* **18**, 930-936, (2021).
877 81 Zhong, E. D., Bepler, T., Berger, B. & Davis, J. H. CryoDRGN: reconstruction of
878 heterogeneous cryo-EM structures using neural networks. *Nat Methods* **18**, 176-185,
879 (2021).
880 82 Radermacher, M. Three-dimensional reconstruction of single particles from random and
881 nonrandom tilt series. *J Electron Microsc Tech* **9**, 359-394, (1988).
882 83 Newcomb, W. W., Homa, F. L., Thomsen, D. R., Ye, Z. & Brown, J. C. Cell-free assembly
883 of the herpes simplex virus capsid. *J Virol* **68**, 6059-6063, (1994).
884 84 Davison, M. D., Rixon, F. J. & Davison, A. J. Identification of genes encoding two capsid
885 proteins (VP24 and VP26) of herpes simplex virus type 1. *J Gen Virol* **73 (Pt 10)**, 2709-
886 2713, (1992).
887 85 Preston, V. G. *et al.* Efficient herpes simplex virus type 1 (HSV-1) capsid formation
888 directed by the varicella-zoster virus scaffolding protein requires the carboxy-terminal
889 sequences from the HSV-1 homologue. *J Gen Virol* **78 (Pt 7)**, 1633-1646, (1997).
890 86 Yuan, S. *et al.* Cryo-EM structure of a herpesvirus capsid at 3.1 A. *Science* **360**, (2018).

891 87 Zhou, Z. H. *et al.* Assembly of VP26 in herpes simplex virus-1 inferred from structures of
892 wild-type and recombinant capsids. *Nat Struct Biol* **2**, 1026-1030, (1995).
893 88 Cardone, G., Heymann, J. B., Cheng, N., Trus, B. L. & Steven, A. C. Procapsid assembly,
894 maturation, nuclear exit: dynamic steps in the production of infectious herpesvirions. *Adv*
895 *Exp Med Biol* **726**, 423-439, (2012).
896 89 Zhang, Z. *et al.* Genome-wide mutagenesis reveals that ORF7 is a novel VZV skin-tropic
897 factor. *PLoS Pathog* **6**, e1000971, (2010).
898 90 Chaudhuri, V., Sommer, M., Rajamani, J., Zerboni, L. & Arvin, A. M. Functions of
899 Varicella-zoster virus ORF23 capsid protein in viral replication and the pathogenesis of
900 skin infection. *J Virol* **82**, 10231-10246, (2008).
901 91 Nicholson, P. *et al.* Localization of the herpes simplex virus type 1 major capsid protein
902 VP5 to the cell nucleus requires the abundant scaffolding protein VP22a. *J Gen Virol* **75 (**
903 **Pt 5)**, 1091-1099, (1994).
904 92 Newcomb, W. W. *et al.* Assembly of the herpes simplex virus capsid: characterization of
905 intermediates observed during cell-free capsid formation. *J Mol Biol* **263**, 432-446, (1996).
906 93 Visalli, M. A., House, B. L., Selariu, A., Zhu, H. & Visalli, R. J. The varicella-zoster virus
907 portal protein is essential for cleavage and packaging of viral DNA. *J Virol* **88**, 7973-7986,
908 (2014).
909 94 Visalli, R. J. & Howard, A. J. Non-axial view of the varicella-zoster virus portal protein
910 reveals conserved crown, wing and clip architecture. *Intervirology* **57**, 121-125, (2014).
911 95 Draganova, E. B., Zhang, J., Zhou, Z. H. & Heldwein, E. E. Structural basis for capsid
912 recruitment and coat formation during HSV-1 nuclear egress. *Elife* **9**, (2020).
913 96 Yang, K. & Baines, J. D. Selection of HSV capsids for envelopment involves interaction
914 between capsid surface components pUL31, pUL17, and pUL25. *Proc Natl Acad Sci U S*
915 *A* **108**, 14276-14281, (2011).
916 97 Mettenleiter, T. C., Muller, F., Granzow, H. & Klupp, B. G. The way out: what we know
917 and do not know about herpesvirus nuclear egress. *Cell Microbiol* **15**, 170-178, (2013).
918 98 Prazak, V. *et al.* Molecular plasticity of herpesvirus nuclear egress analysed in situ. *Nat*
919 *Microbiol* **9**, 1842-1855, (2024).

920 99 Klupp, B. G., Granzow, H. & Mettenleiter, T. C. Nuclear envelope breakdown can
921 substitute for primary envelopment-mediated nuclear egress of herpesviruses. *J Virol* **85**,
922 8285-8292, (2011).
923 100 Dai, X. *et al.* The smallest capsid protein mediates binding of the essential tegument protein
924 pp150 to stabilize DNA-containing capsids in human cytomegalovirus. *PLoS Pathog* **9**,
925 e1003525, (2013).
926 101 Tischer, B. K. *et al.* A self-excisable infectious bacterial artificial chromosome clone of
927 varicella-zoster virus allows analysis of the essential tegument protein encoded by ORF9.
928 *J Virol* **81**, 13200-13208, (2007).
929 102 Yang, E., Arvin, A. M. & Oliver, S. L. The cytoplasmic domain of varicella-zoster virus
930 glycoprotein H regulates syncytia formation and skin pathogenesis. *PLoS Pathog* **10**,
931 e1004173, (2014).
932 103 Wolff, G. *et al.* Mind the gap: Micro-expansion joints drastically decrease the bending of
933 FIB-milled cryo-lamellae. *J Struct Biol* **208**, 107389, (2019).
934 104 Mastronarde, D. N. Automated electron microscope tomography using robust prediction
935 of specimen movements. *J Struct Biol* **152**, 36-51, (2005).
936 105 Tegunov, D. & Cramer, P. Real-time cryo-electron microscopy data preprocessing with
937 Warp. *Nat Methods* **16**, 1146-1152, (2019).
938 106 Mastronarde, D. N. Dual-axis tomography: an approach with alignment methods that
939 preserve resolution. *J Struct Biol* **120**, 343-352, (1997).
940 107 Kremer, J. R., Mastronarde, D. N. & McIntosh, J. R. Computer visualization of three-
941 dimensional image data using IMOD. *J Struct Biol* **116**, 71-76, (1996).
942 108 Pettersen, E. F. *et al.* UCSF ChimeraX: Structure visualization for researchers, educators,
943 and developers. *Protein Sci* **30**, 70-82, (2021).
944 109 Jumper, J. *et al.* Highly accurate protein structure prediction with AlphaFold. *Nature* **596**,
945 583-589, (2021).
946 110 Phillips, J. C. *et al.* Scalable molecular dynamics on CPU and GPU architectures with
947 NAMD. *J Chem Phys* **153**, 044130, (2020).
948 111 Croll, T. I. ISOLDE: a physically realistic environment for model building into low-
949 resolution electron-density maps. *Acta Crystallogr D Struct Biol* **74**, 519-530, (2018).
950

ACKNOWLEDGMENTS

Cryo-FIB-SEM and cryo-ET were performed at the Stanford-SLAC Cryo-EM Center and the Stanford-SLAC Cryo-ET Specimen Preparation Center under the support of the National Institutes of Health Common Fund's Transformative High Resolution Cryo-electron Microscopy Program (U24GM139166 and U24GM129541); and the NIH Shared Instrumentation Grant (S10OD021600). Research support was provided by NIH grants R01AI020459 (SLO), R21AI159375 (SLO and WC), R01GM150905 (MC), AI15937502 (WC), and R21MH125285 (MC). Molecular graphics and analyses performed with UCSF ChimeraX, developed by the Resource for Biocomputing, Visualization, and Informatics at the University of California, San Francisco, with support from National Institutes of Health R01GM129325 and the Office of Cyber Infrastructure and Computational Biology, National Institute of Allergy and Infectious Diseases.

AUTHOR CONTRIBUTIONS

SLO: Conceptualization, methodology, software application, validation, formal analysis, investigation, resources, data curation, writing - original draft and editing, visualization, supervision, project administration, funding acquisition. MC: Software application, validation, formal analysis, writing - review and editing. LE: Methodology, resources, writing - review and editing. CWH: Methodology, writing - review and editing. XZ: Methodology, writing - review and editing. MFS: Validation, formal analysis, writing - review and editing. AMA: Resources, writing - review and editing, supervision, funding acquisition. WC: Resources, writing - review and editing, supervision, funding acquisition.

COMPETING INTERESTS

The authors declare no competing interests.

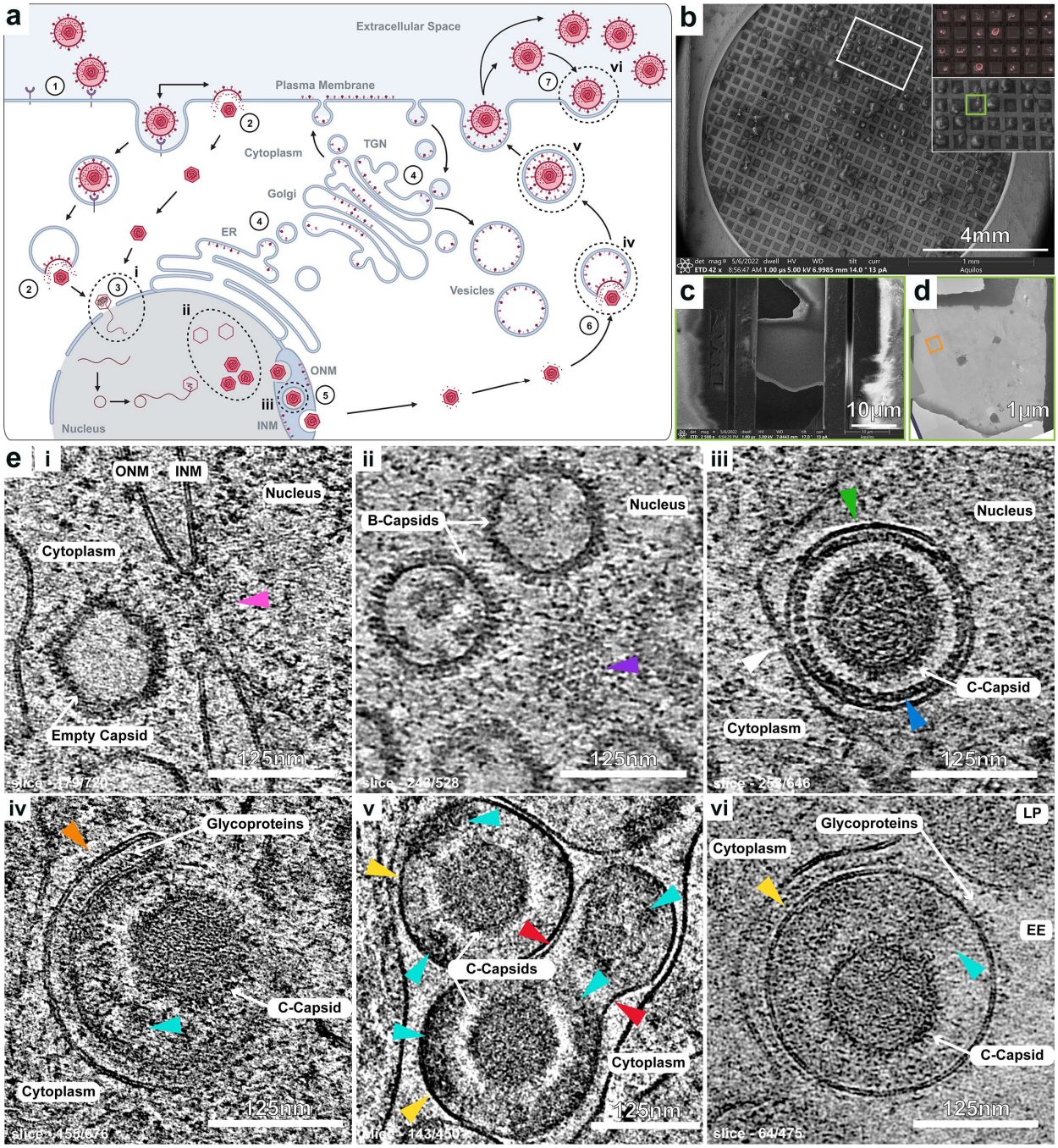

Figure 1. The VZV replication cycle and stages of morphogenesis within infected MeWo cells in 3D space captured by cryo-FIB/cryo-ET. (a) A cartoon representation (drawn using Biorender) of the VZV replication cycle where the key steps are numbered from 1 through 7 (black circles). VZV glycoproteins bind cell surface receptors during virion attachment (1), allowing the gB/gH-gL fusion complex to fuse the envelope with cell membranes either in endocytic vesicles or directly with the plasma membrane (2). The capsid is released into the cytoplasm, traffics to and docks with a nuclear pore where the dsDNA genome is injected into the cell nucleus (3) to initiate replication and capsid assembly. VZV glycoproteins necessary for attachment and cell

983 entry, are synthesized in the endoplasmic reticulum (ER) and trafficked to the Golgi during
984 maturation, exocytosed then endocytosed and trafficked to the trans-Golgi network (TGN) or
985 trafficked to the nuclear envelope (inner nuclear membrane, INM; outer nuclear membrane, ONM)
986 (4). Newly synthesized capsids undergo nuclear egress through the nuclear envelope via
987 envelopment and de-envelopment courtesy of the nuclear egress complex (5). Glycoproteins are
988 trafficked from the TGN to sites of secondary envelopment, where capsids acquire additional
989 tegument proteins, and incorporated into nascent virus particles (6). VZV particles are exported in
990 vesicular structures to the extracellular environment (7) where they can either be released into the
991 extracellular environment or attach to the plasma membrane. **(b)** Cryogenic scanning electron
992 microscopy (cryo-SEM) of VZV infected MeWo cells seeded on a micropatterned Quantifoil 300
993 mesh SiO_2 grid. The inset shows a zoomed in image of fluorescence microscopy (right top) of the
994 grid prior to vitrification (red fluorescence indicates infection with recombinant VZV expressing
995 TK-RFP) and the cryo-SEM image post vitrification (right bottom). The green square highlights
996 a single cell where a lamella was milled and presented in panels **c** and **d**. **(c)** A lamella produced
997 by cryo-FIB milling of the VZV infected cell highlighted in A. **(d)** A montage image
998 (16.85Å/pixel) produced by cryogenic transmission electron microscopy (cryo-TEM) of the
999 lamella from panel **C**. The inset orange box highlights the zoomed in area where tilt series data
1000 were collected to generate the tomogram in panel Ev. **(e)** In our cryo-FIB/cryo-ET data, we have
1001 captured capsids corresponding to some of the VZV replication stages labeled in Roman numbers
1002 (i-vi) and outlined by dotted black ellipses in panel A. Each image is a single slice through a low
1003 pass filtered tomogram. **(i)** An empty VZV capsid is visible at the nuclear pore where the inner
1004 and outer nuclear membrane converge (pink arrowhead). **(ii)** B-capsids containing scaffold protein
1005 and the capsomeres of an adjacent capsid along the 3-fold axis (blue violet arrowhead). **(iii)** A C-
1006 capsid surrounded by the nuclear egress complex (navy blue arrowhead) and the primary envelope
1007 (lime green arrowhead) undergoing fusion with the outer nuclear membrane (white arrowhead).
1008 **(iv)** A C-capsid interacting with the tegument layer (bright turquoise arrowhead) and glycoprotein-
1009 coated cell membranes (tangerine arrowhead) morphing around the capsid-tegument complex. **(v)**
1010 VZV particles containing C-capsids, one that has undergone complete morphogenesis and a second
1011 in the process of the final steps of morphogenesis and the production of a light particle. The
1012 tegument is clearly visible as the dark structures (bright turquoise arrowheads) between the capsids
1013 and the VZV particle envelope (gorse yellow arrowheads). Red arrowheads indicate a point of
1014 constriction between the formation of a complete VZV particle and a light particle. **(vi)** VZV
1015 particles released into the extracellular environment (EE) bound to the plasma membrane. One
1016 contains a C-capsid with the tegument (bright turquoise arrowheads) clearly visible as the dark
1017 structures between the capsids and the VZV particle envelope (gorse yellow arrowheads), which
1018 is coated with glycoproteins. The second is a partially visible light particle (LP) also bound to the
1019 plasma membrane. Scale bars 125nm.
1020

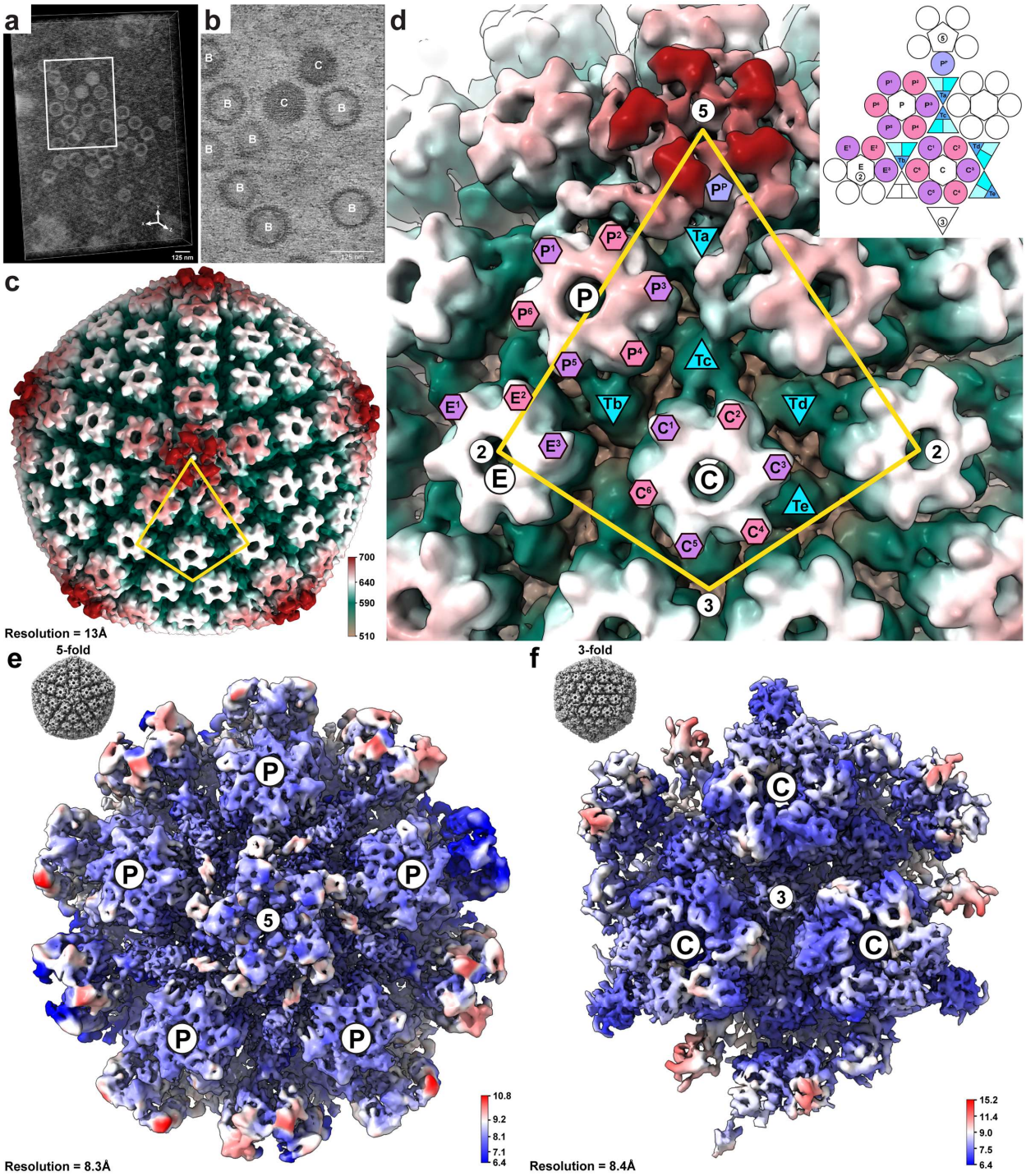

Figure 2. Cryo-ET density maps of the VZV capsid, capsid vertex, and the 3-fold symmetry axis. (a) A representative tomogram reconstruction produced from cryo-ET of a cryo-FIB/SEM milled region inside the nucleus of a vitrified, VZV infected MeWo cell represented as a 3D-volume. **(b)** A single slice from the tomogram in (**a**) in a region inside the nucleus of a vitrified VZV infected MeWo cell where a cluster of B-capsids (scaffold protein and without dsDNA labeled as B) and C-capsids (dsDNA genome labeled as C) were identified. Scale bars indicate 125nm. **(c)** Surface representation of a cryo-ET map (13Å) generated by subtomogram averaging

with imposed icosahedral symmetry of 317 VZV capsids with a mixture of B and C capsids. The capsid is colored radially (510-700Å form the center of the capsid). The yellow kite connects the 2-, 3-, and 5-fold axes of symmetry. **(d)** Zoom in view of a portion of (**c**) annotated with protein components that make up an asymmetric unit composed of the pentonal major capsid protein (P^P), the three types of hexon (peripentonal (P1-P6), edge (E1-E3), and center (C1-C6)), and the five triplexes (Ta, Tb, Tc, Td, and Te). The inset (right) is a schematic of the asymmetric unit of the icosahedral capsid. **(e and f)** Cryo-ET maps generated by subtomogram averaging and focused classification of the VZV capsid vertex (e; 8.3Å; EMD-49591) and 3-fold axis of symmetry (f; 8.4Å; EMD-49886). The inset cryo-ET maps of the 13Å VZV capsid cryo-ET map are projected along the 5-fold (**e**) and 3-fold (**f**) axes of symmetry. Peripentonal (P) and center (C) hexons are labelled. The color key indicates the local resolution (Å) of the cryo-ET maps.

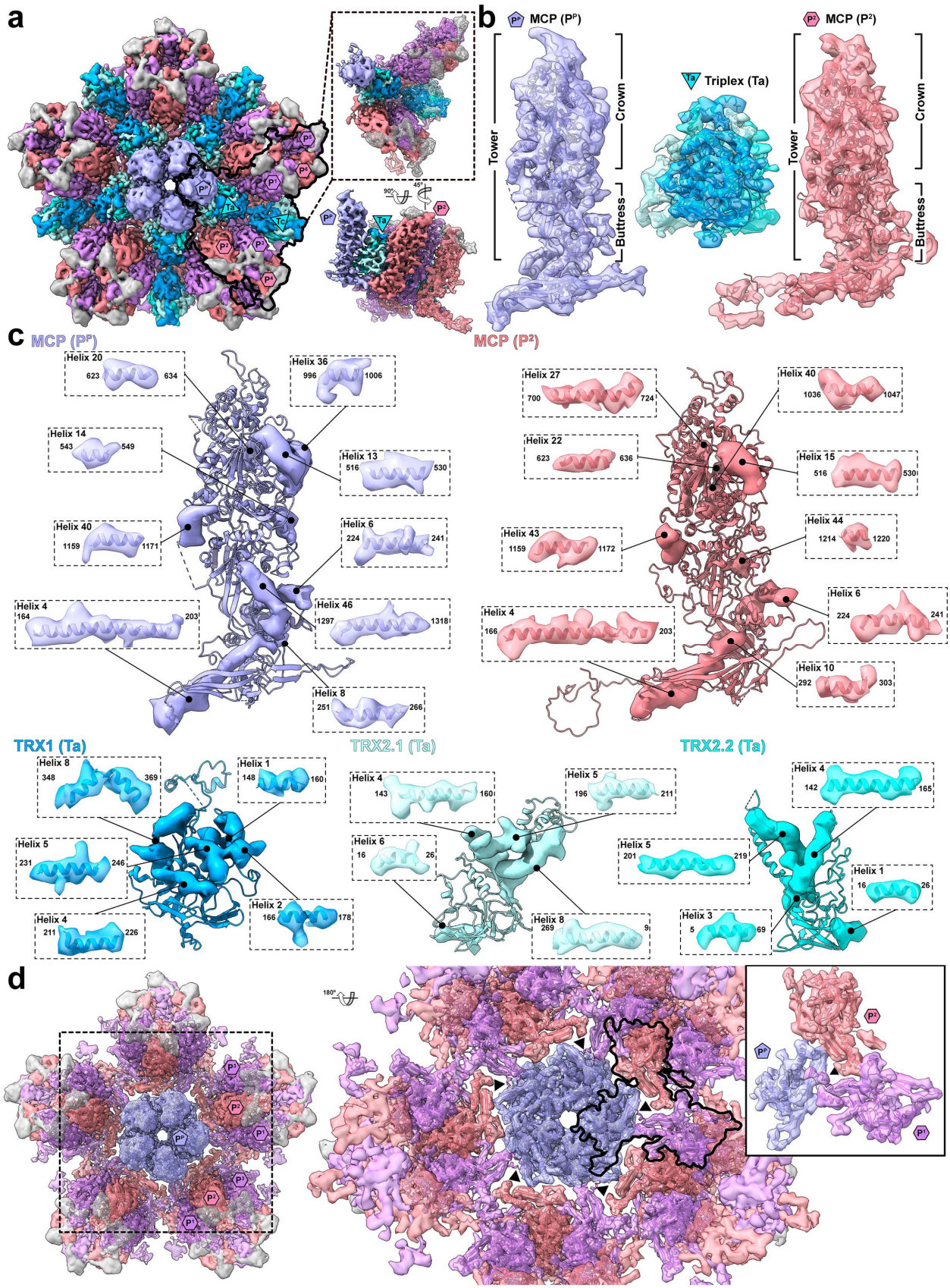
a
b
MCP (P¹)
Triplex (Ta)
MCP (P²)
Tower
Crown
Buttress
c
MCP (P¹)
MCP (P²)
Helix 20
Helix 36
Helix 14
Helix 13
Helix 40
Helix 6
Helix 4
Helix 46
Helix 8
Helix 27
Helix 40
Helix 22
Helix 15
Helix 43
Helix 44
Helix 6
Helix 4
Helix 10
TRX1 (Ta)
TRX2.1 (Ta)
TRX2.2 (Ta)
Helix 8
Helix 1
Helix 5
Helix 4
Helix 2
Helix 4
Helix 5
Helix 6
Helix 8
Helix 4
Helix 5
Helix 1
Helix 3
d

1041

1042 **Figure 3. Segmentation of the 8.3Å VZV capsid vertex cryo-ET map. (a)** Segmentation of
1043 the 8.3Å cryo-ET map based on the 7BW6[39] and a refined model based on the subnanometer map.
1044 The major capsid protein (MCP; ORF40) of the penton (P^P) and the peripentonal hexons (P^{1-6}),
1045 triplex proteins TRX1 (ORF20) and TRX2 (ORF41) for triplexes Ta and Tc, and small capsomere
1046 interacting protein (SCP; ORF23) are colored lavender blue (P^P), very soft violet ($P^{1,3,5}$), light coral
1047 ($P^{2,4,6}$), deep sky blue (TRX1), Columbia blue (TRX2.1), aqua (TRX2.2), and dark gray (SCP).
1048 The colored shapes within the black outline demarcate a portion of the asymmetric unit (P^P, P^{1-6}
1049 and associated SCP, and triplexes Ta and Tc) of the VZV capsid vertex, which is isolated in the
1050 dotted box (inset). **(b)** Extracted densities of the P^P and P^2 MCP with the tower, buttress and
1051 crown highlighted, and Ta triplex. **(c)** Exploded views of extracted densities for helices from the
1052 P^P and P^2 MCP, and Ta triplex. Each helix is numbered according to the primary structure along
1053 with the beginning and end numbered amino acids. **(d)** Segmentation of the VZV capsid vertex
1054 without the triplexes. P^P and P^{1-3} MCPs are identified with colored shapes. The dashed boxed
1055 outlines the region shown in the right hand panel. Triangles represent the local 3-fold symmetry
1056 axes where the pentonal MCP (P^P) intersects the two peripentonal hexon MCPs, P^1 and P^2. The
1057 black outline highlights the intersection between the HK97-like fold and the P^P, P^1, and P^2 MCPs
1058 (inset).
1059

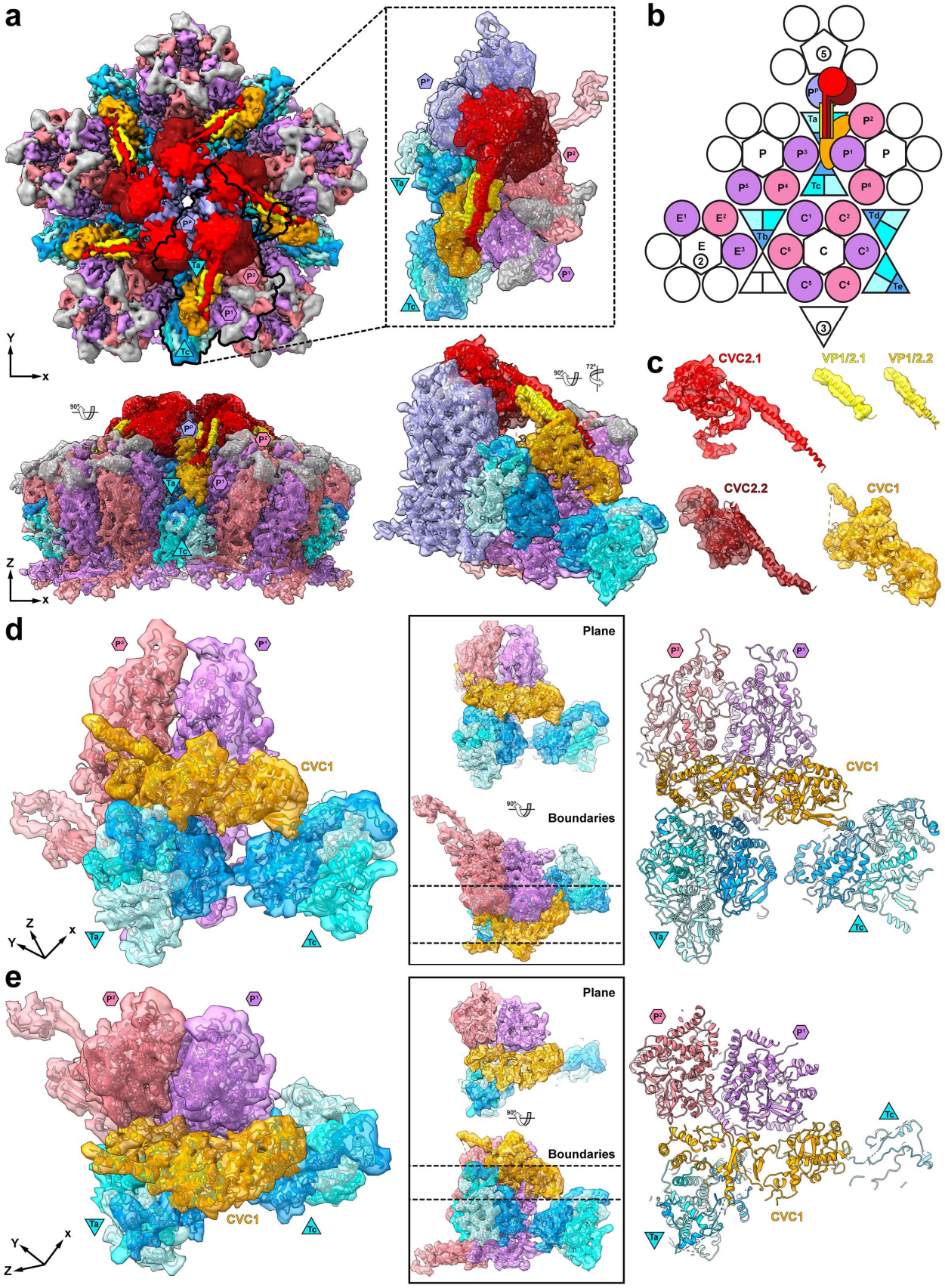
a
b
c
d
e
CVC2.1
VP1/2.1
VP1/2.2
CVC2.2
CVC1
Plane
Boundaries
Ta
Tb
Tc
Td
Te

1060

1061 **Figure 4. The VZV capsid vertex specific component redefines the asymmetric unit. (a)**
1062 Segmentation of the 8.3Å cryo-ET map of the vertex around the 5-fold axis of the capsid to isolate
1063 the CVSC and fit an AlphaFold 2 model using MDFF simulation and the 7BW6[39] model. The
1064 MCP, SCP, TRX1, and TRX2 are colored as for Fig. 3 and the CVSC subunits colored orange
1065 (CVC1; ORF43), red (CVC2.1; ORF34), falu red (CVC2.2; ORF34), yellow (VP1/2.1; ORF22),
1066 and gold (VP1/2.2; ORF22). The black outline highlights a portion of the VZV capsid vertex with
1067 the CVSC, which is isolated in the dashed box (inset). The lower panels show side views of the
1068 complete vertex map and the extracted region in the dotted box. **(b)** A cartoon representing the
1069 CVSC components' locations in relation to the redefined asymmetric unit compared to Fig 2C.
1070 Colored shapes define the pentonal major capsid protein (P^P), the three types of hexon
1071 (peripentonal (P^1-P^6), edge (E^1-E^3), and center (C^1-C^6)), the five triplexes (Ta, Tb, Tc, Td, and Te),
1072 and the CVSC. **(c)** Exploded view of the CVSC subunits. **(d and e)** Extracted densities revealing
1073 (**d**) CVC1 (ORF43) interactions with triplexes Ta and Tc, and (**e**) peripentonal hexon MCP P^1 and
1074 P^2. Models of the CVC1, TRX1, TRX2, P^1, and P^2 within the cryo-ET map densities are shown
1075 in the left-hand panels. Right hand panels show plane views of the molecular models (far right)
1076 that highlight likely interaction sites between CVC1, the triplexes (**d**), and peripentonal MCPs (**e**)
1077 and the boundaries of the planes (black boxes).
1078

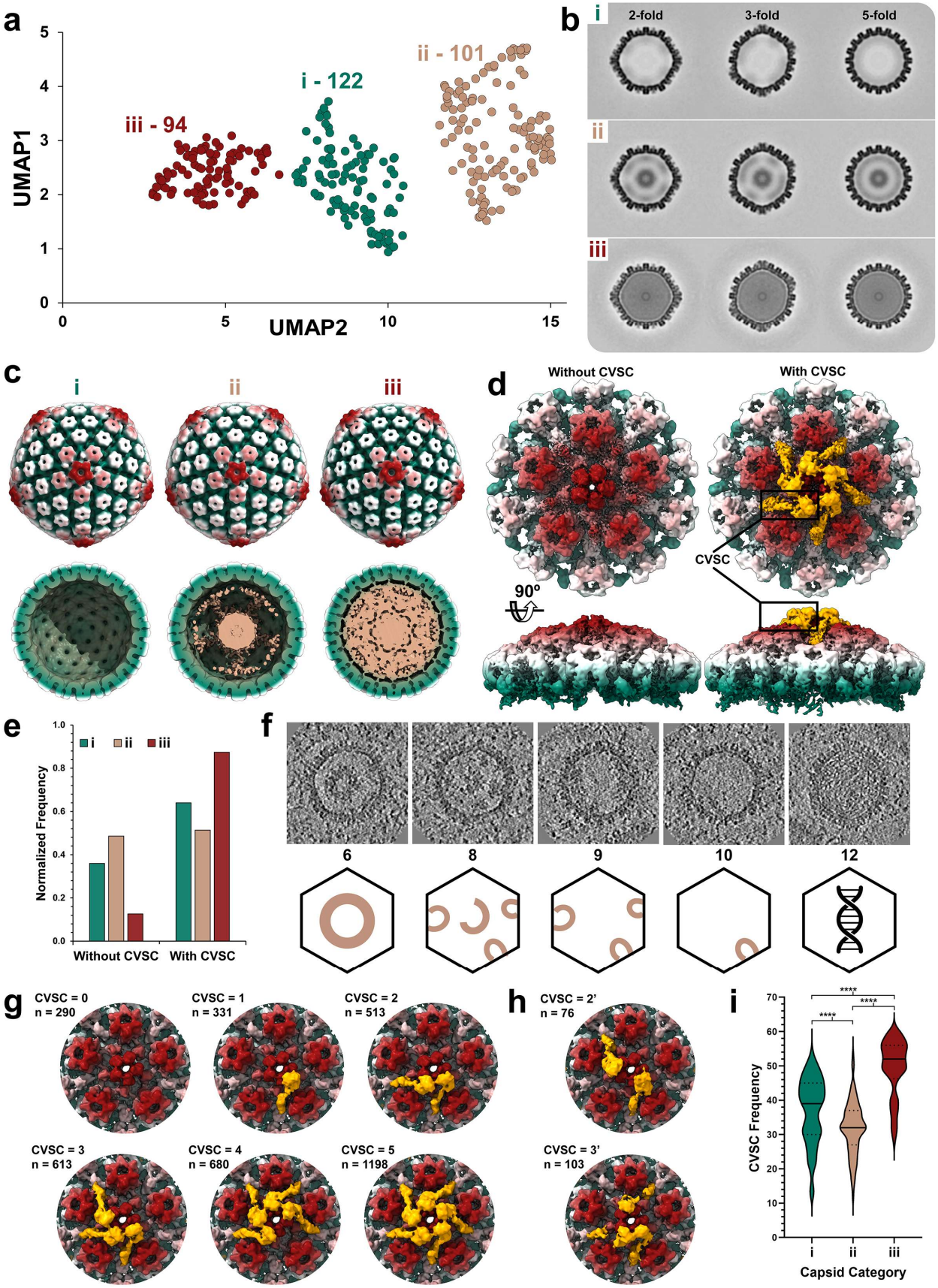
a
UMAP1
UMAP2
iii - 94
i - 122
ii - 101
b
i
ii
iii
2-fold
3-fold
5-fold
c
i
ii
iii
d
Without CVSC
With CVSC
CVSC
90º
e
i
ii
iii
Normalized Frequency
Without CVSC
With CVSC
f
6
8
9
10
12
g
CVSC = 0
n = 290
CVSC = 1
n = 331
CVSC = 2
n = 513
CVSC = 3
n = 613
CVSC = 4
n = 680
CVSC = 5
n = 1198
h
CVSC = 2'
n = 76
CVSC = 3'
n = 103
i
CVSC Frequency
Capsid Category

1079

1080 **Figure 5. The capsid vertex specific component as a temporal marker for herpesvirus**
1081 **capsid assembly. (a)** Uniform manifold approximation and projection (UMAP) of 317 VZV
1082 capsids producing three clusters, i, ii and iii. **(b)** 2D class averages of clusters i to iii projected
1083 along 2-, 3-, and 5-fold axes of symmetry. **(c)** Subtomogram reconstruction of the three capsid
1084 classes, i, ii, and iii. Capsids are colored radially from the center of the capsid to the outer shell;
1085 beige, green, white, and red. The transverse planes show the empty cavity, (i), scaffold filled cavity
1086 (ii), and DNA filled cavity (iii) of the VZV capsids. **(d)** Subtomogram reconstructions of the
1087 capsid vertex without and with the CVSC. The vertices are colored radially as for panel B with
1088 the CVSC colored yellow. **(e)** Normalized frequency of i, ii, and iii capsid classes without or with
1089 the CVSC. **(f)** Increased CVSC occupancy at capsid vertices associated with decreased scaffold
1090 protein. Slice view of representative polished particles (EMAN2) extracted from tomograms and
1091 cartoons depicting the scaffold protein visible in the capsid cavity. Numbers represent the
1092 frequency of vertices occupied with the CVSC. **(g)** Subtomogram averaging after symmetry
1093 relaxation and focused classification. The frequency (n) of VZV capsid vertices without (0) or
1094 with 1 to 5 copies of the CVSC (yellow) is indicated for each vertex. **(h)** Non-consecutive
1095 distribution of the CVSC (yellow) at the VZV capsid vertices with the frequency (n) of 2 (2') or 3
1096 (3') copies after subtomogram averaging and focused classification. **(i)** A violin plot representing
1097 the frequency of the CVSC (60 copies per capsid; 5 CVSC subunits per 12 vertices of the capsid)
1098 for each capsid class, i, ii and iii. The solid line represents the median and the dotted lines represent
1099 quartiles. Asterisks above the violin plots indicate p-values (<0.0001) for significant differences
1100 from a Tukey's multiple comparison test.

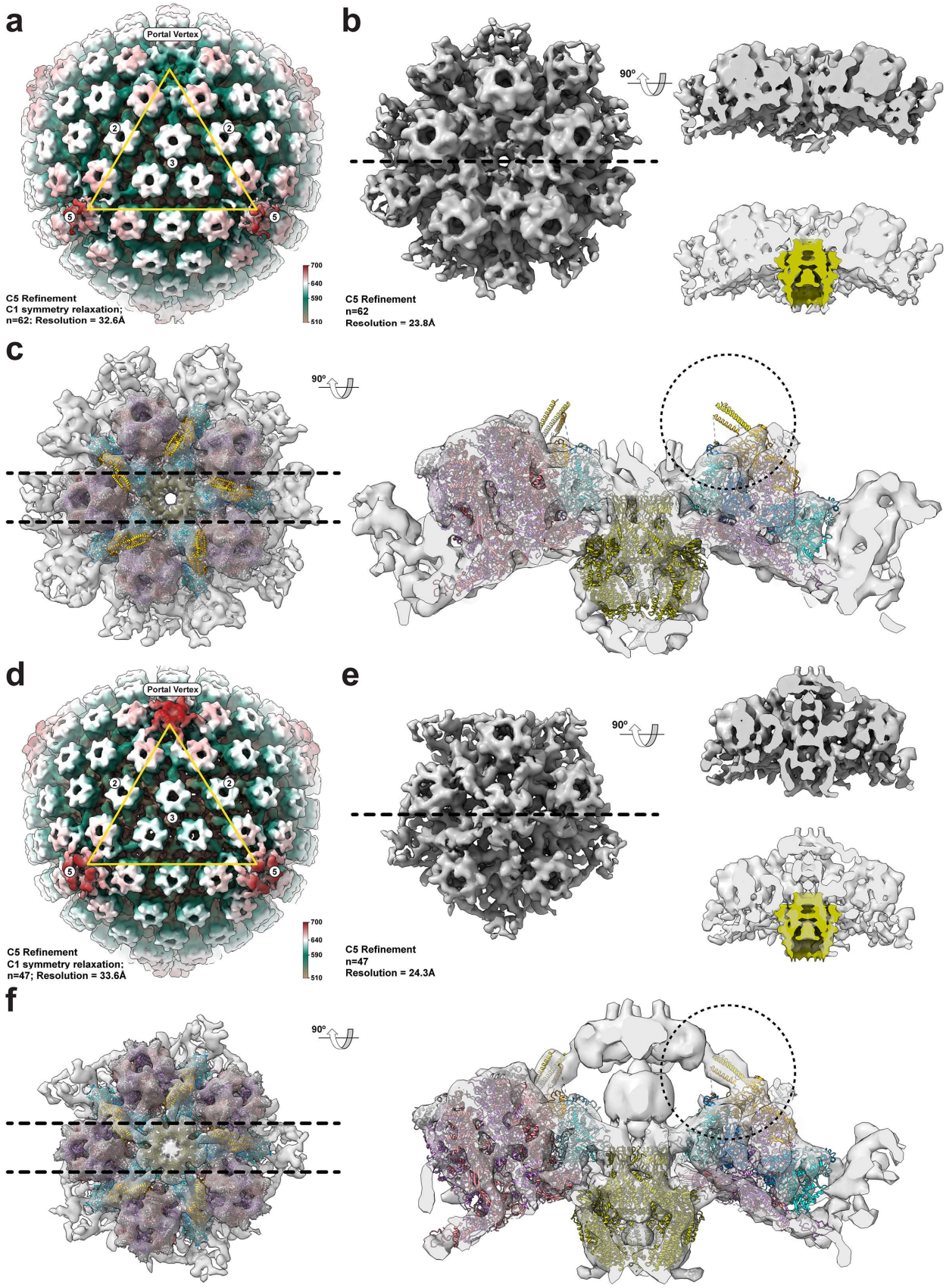
a
Portal Vertex
2
2
3
5
5
700
640
590
510
C5 Refinement
C1 symmetry relaxation;
n=62; Resolution = 32.6Å
b
90°
C5 Refinement
n=62
Resolution = 23.8Å
c
90°
d
Portal Vertex
2
2
3
5
5
700
640
590
510
C5 Refinement
C1 symmetry relaxation;
n=47; Resolution = 33.6Å
e
90°
C5 Refinement
n=47
Resolution = 24.3A
f
90°

1101

1102 **Figure 6. Differences in portal vertex architecture between VZV CAIs and C-capsids. (a to**
1103 **f)** Cryo-ET maps of CAI and C-capsids and their portal vertices. **(a and d)** Cryo-ET maps of the
1104 VZV CAIs (A; EMD-49470) and C-capsid (D; EMD-49472) projected along the 3-fold axis of
1105 symmetry and colored radially (510-700Å form the center of the capsid). The yellow triangle
1106 encompasses the 2-, 3-, and 5-fold axes of symmetry. **(b and e)** Cryo-ET maps of the portal
1107 vertices from CAIs (B; EMD-49471) and C-capsids (E; EMD-49473). The left-hand panels show
1108 the vertices along the Z-axis of the cryo-ET map. The dashed black line shows the slice for views
1109 along the Y-axis, upper right-hand panels. The lower right-hand panels for the CAIs and C-capsids
1110 show transparent views of the cryo-ET maps with the portal map (see Suppl. Fig 15) aligned to the
1111 portal vertex map density. **(c and f)** The molecular model of the VZV capsid vertex without the
1112 pentonal MCP was fit into the cryo-ET maps of the CAIs and C-capsid portal vertices. The MCP
1113 of peripentonal hexons, triplexes Ta and Tc (TRX1, TRX2.1, and TRX2.2), small capsomere
1114 interacting protein (SCP), CVSC subunits CVC1, VP1/2.1 and VP1/2.2, and the VZV portal
1115 protein ORF54 are colored light coral or very soft violet (MCP), deep sky blue (TRX1), Columbia
1116 blue (TRX2.1), aqua (TRX2.2), dark gray (SCP), orange (CVC1), yellow (VP1/2.1), gold
1117 (VP1/2.2), and olive yellow (ORF54). Dashed lines indicate the slices used for the right-hand
1118 panels to more clearly visualize the portal. The dashed circles highlight the absence of CVSC
1119 densities in the portal vertex cryo-ET map for the B-capsid compared to the C-capsid (right-hand
1120 panels).